Effects of fluid boiling on Au and volatile element enrichment in submarine arc-related hydrothermal systems

Jan J. Falkenberg [a,*], Manuel Keith [a], Karsten M. Haase [a], Wolfgang Bach [b], Reiner Klemd [a], Harald Strauss [c], Isobel A. Yeo [d,e], Kenneth H. Rubin [f], Bettina Storch [a], Melissa O. Anderson [g]

[a] *GeoZentrum Nordbayern, Friedrich-Alexander-Universität (FAU) Erlangen-Nürnberg, 91054 Erlangen, Germany*
[b] *MARUM – Centre for Marine Environmental Sciences and Faculty of Geoscience University of Bremen, Bremen, Germany*
[c] *Institut für Geologie und Paläontologie, Universität Münster, Münster 48149, Germany*
[d] *National Oceanography Centre Southampton, European Way, Southampton SO14 3ZH, UK*
[e] *GEOMAR, Helmholtz Center for Ocean Research Kiel, Wischhofstraße 1-3, 24148 Kiel, Germany*
[f] *Department of Geology and Geophysics, University of Hawaii, Honolulu, HI 96822, USA*
[g] *Department of Earth Sciences, University of Toronto, 22 Russell Street, Toronto, Ontario M5S3B1, Canada*

Abstract

Shallow (<1500 mbsl) submarine arc-related hydrothermal systems can host base (Cu), precious (Au) and volatile elements (As, Se, Sb, Te, Tl) in significant quantities. Their wide application in the high-tech industry, but a potential eco-toxicological footprint gives them a strategic importance. However, the processes that concentrate these elements in submarine arc-related hydrothermal systems, compared to their mid-ocean ridge counterparts are still debated, and it is unclear whether boiling-related processes and/or the contribution of magmatic volatiles are key for their enrichment.

We present bulk sulfide-sulfate, isotope (S and Pb), and high-resolution microanalytical data of hydrothermal sulfides from the Niua South fore-arc volcano in north Tonga, where numerous black-smoker type sulfide-sulfate chimneys emit boiling fluids with temperatures (up to 325 °C) near the seawater boiling curve at ~1170 m water depth. Hence, this system represents an ideal natural laboratory to investigate the effect of fluid boiling on base, precious, and volatile element enrichment associated with hydrothermal seafloor mineralization. At Niua South, textural and chemical variations of multiple pyrite (framboidal, euhedral and massive), chalcopyrite (linings), and sphalerite (dendrites and linings) generations are indicative for sulfide precipitation from early low-temperature (~240 °C) fluids that underwent abundant mixing with ambient seawater (low Se/Tl and Co/Ni ratios in pyrite) and from later high-temperature (up to 325 °C) (high Se/Tl and Co/Ni ratios in pyrite). In addition, crustiform inclusion-rich pyrite that precipitated from high-temperature boiling fluids shows low Bi/Pb, Tl/Pb and Sb/Pb ratios due to volatile element loss (e.g., Tl and Sb) to the vapor phase compared to pyrite that formed during the low temperature stage. By contrast, late sphalerite (~280 °C) is enriched in elements with an affinity to Cl-complexes like Mn, Co, Ni, Ga, Cd, In, and Sn, and therefore precipitated from the corresponding Cl-rich liquid phase.

Gold occurs in solid-solution and as boiling-induced particles of native Au, electrum, and Au-rich Bi-tellurides in pyrite (up to 144 ppm Au), sphalerite (up to 60 ppm Au), and chalcopyrite (up to 37 ppm Au). These particles (<5–10 μm) probably formed during fluid boiling causing an extreme Au enrichment (>30 ppm) in the mature and late stage of chimney formation. Lead isotope data indicate that the hydrothermal fluids scavenged metals not only from the deeper basement in the reaction zone (20–40%), but also from young dacitic volcanic rocks near the seafloor in the upflow zone (60–80%). Sulfur isotope

---

* Corresponding author at: GeoZentrum Nordbayern, Friedrich-Alexander-Universität Erlangen-Nürnberg, Schlossgarten 5, 91054 Erlangen, Germany.

E-mail address: jan.falkenberg@fau.de (J.J. Falkenberg).

(δ^{34}S = −0.3 to 4.4‰) and Se/S*10^6 values (<1500) of hydrothermal sulfides provide no evidence for a magmatic volatile influx and indicate that S, and most metals and semi-metals were likely leached from the host rocks. Hence, volatile (As, Se, Sb, Te, Tl), and precious (Au) element enrichments in arc-related submarine hydrothermal systems can be decoupled from magmatic volatiles and are instead a result of boiling-induced trace element fractionation – a hydrothermal enrichment process, which has been underestimated to date.

1. INTRODUCTION

More than 700 submarine hydrothermal vent sites have been found since the discovery of high temperature hydrothermal black smokers venting at the Galápagos Rift in 1979 (Corliss et al., 1979) including about 300 associated with arc and back-arc volcanism, and more than 400 along mid-ocean ridges (Hannington et al., 2005, 2011; Beaulieu and Szafrański, 2020). Hydrothermal sulfides in arc-related settings are enriched in economically important (e.g., Cu, Sb, Au) but also in eco-toxicological (e.g. As, Hg, Tl) elements compared to their mid-ocean ridge counterparts (Monecke et al. 2016; Kilias et al., 2013; Fuchs et al., 2019). These sites are suggested to be modern analogues for ophiolite-hosted volcanogenic massive sulfide (VMS) deposits (Franklin et al., 2005; Martin et al., 2019). World-class VMS deposits have been mined on land for centuries, however fractionation and enrichment processes for many trace and semi-metals are still poorly constrained (Martin et al., 2019, 2020). In order to better understand the major ore-forming processes and element fractionations, high-resolution microanalytical work in actively forming submarine hydrothermal mineralizations represents a unique opportunity to sample the ore-forming fluids and the associated sulfide precipitates.

Hydrothermal circulation along mid-ocean ridges is driven by a magmatic heat source producing hot (up to 400 °C) acidic (pH = 3–4) hydrothermal fluids (modified seawater) that can effectively leach metals from the igneous host rocks in the reaction- and upflow zone (Franklin et al., 2005; Hannington et al., 2005; Tivey, 2007). By contrast, the metal and semi-metal budget (e.g., Cu, As, Se, and Au) of hydrothermal fluids and sulfide precipitates in arc-related settings may strongly be affected by the influx of magmatic volatiles (Herzig et al., 1998; Yang and Scott, 2006; de Ronde et al., 2011, 2019; Keith et al., 2018b; Martin et al., 2020). Mixing of hydrothermal fluids with ambient cold seawater causes metal and semi-metal precipitation due to drastic changes in temperature, pH and redox conditions (e.g., Tivey et al., 1999; Berkenbosch et al., 2012; Wohlgemuth-Ueberwasser et al., 2015; Keith et al., 2016; Meng et al., 2020). In addition, pressure-dependent fluid boiling is a common process in shallow (<1500 mbsl) submarine arc-related hydrothermal systems causing element fractionation between the segregating liquid- and vapor-fluid phase (Reed, 2006; Pokrovski et al., 2013; Monecke et al., 2014; Keith et al., 2021), which may be preserved by the texture

and composition of associated sulfide precipitates (Tardani et al., 2017; Keith et al., 2020; Reich et al., 2020). For instance, elements like As, Se, Sb, Te, Hg, and Tl preferentially partition into the vapor phase, whereas Mn, Fe, Co, Ni, Zn, Sn, and Pb are concentrated in the liquid phase due to their affinity to form Cl-complexes (Pokrovski et al., 2013; Román et al., 2019). By contrast, Au precipitates during fluid boiling caused by H_2S loss to the vapor phase and the destabilization of the Au bisulfide-complex, which may be a critical process for the Au enrichment in epithermal (Cooke and McPhail, 2001; Pokrovski et al., 2014; Keith et al., 2018a, 2020), geothermal (Simmons and Brown, 2007; Hannington et al., 2016; Libbey and Williams-Jones, 2016) and submarine hydrothermal systems (Gartman et al., 2018; Fuchs et al., 2019).

Pyrite is the most abundant sulfide mineral in many submarine hydrothermal systems and an important host for a wide range of trace elements (e.g., Co, Ni, As, Se, Mo. Ag, Cd, Sb, Te, Au, Tl, and Pb) (Wohlgemuth-Ueberwasser et al., 2015; Keith et al., 2016). Pyrite forms under various fluid conditions and, thus, its chemical composition may provide insight into various hydrothermal processes including fluid boiling (Maslennikov et al., 2009; Keith et al., 2016, 2018a; Martin et al., 2019, 2020; Román et al., 2019). Sphalerite, on the other hand, represents a useful tool to estimate precipitation temperatures and sulfidation states based on its Fe content, as well as its Fe/Zn and Ga/Ge ratios (Möller, 1987; Einaudi et al., 2003; Keith et al., 2014; Kawasumi and Chiba, 2017). By contrast, the composition of chalcopyrite reflects the high temperature (300–400 °C) stage during the evolution of a vent systems, possibly related to chalcopyrite-fluid equilibrium conditions (Butler and Nesbitt, 1999; McDermott et al., 2015; Wohlgemuth-Ueberwasser et al., 2015; Evans et al., 2020; Meng et al., 2020). The radiogenic Pb and stable S isotope composition of these sulfides is used to define the source components in hydrothermal systems, namely leaching of metals from the host rocks and the potential contribution of magmatic volatiles (Fouquet and Marcoux, 1995; Herzig et al., 1998; Ono et al., 2007; McDermott et al., 2015; Zeng et al., 2017; Martin et al., 2020).

Here, we present bulk sulfide-sulfate data coupled with in-situ trace element, as well as Pb and S isotope analyses of pyrite, sphalerite, and chalcopyrite, which provide important new insights into the hydrothermal mineralization processes in boiling submarine arc-related hydrothermal systems. This study unravels the interplay

between physicochemical fluid parameters (e.g., temperature, salinity, fO_2, fS_2), fluid boiling and influx of magmatic volatiles, and reveal their impact on sulfide chemistry, thereby ultimately providing a comprehensive framework for the boiling-induced enrichment of precious (Au) and volatile (As, Se, Sb, Te, and Tl) elements in submarine arc-related hydrothermal systems.

2. GEOLOGICAL SETTING AND SAMPLING LOCALITIES

The Tonga-Kermadec arc is a 2500 km long chain of active, mostly submarine volcanoes in the western Pacific Ocean (Fig. 1A). The northernmost part of the Tonga arc (Tofua arc) has the highest subduction rates (240 mm/yr at 16°S) on earth and numerous arc front, rear-arc and back-arc volcanoes formed through the westward subduction of the Pacific Plate beneath the Indo-Australian Plate (Bevis et al., 1995; Smith and Price, 2006; Embley and Rubin, 2018).

The rhombohedral shaped, highly tectonized, Niua volcanic complex (formerly "Volcano P") is the northernmost volcanic structure of the Tofua arc and is suggested to have been inactive for several thousand years (Rubin et al., 2013). It has been previously divided into Niua North and Niua South based on physiographic features (Fig. 1B) (Arculus, 2006; Lupton, 2008; Merle et al., 2012; Rubin et al., 2013; Kwasnitschka, 2016). Igneous rocks at the Niua volcanic complex span a limited compositional range from andesites to rhyolites (Falloon et al., 2007; Haase, 2018) with typical arc-like trace element and volatile element abundances (Falloon et al., 2007; Lupton et al., 2015). Hydrothermal activity at Niua South was first examined on the NOAA Ocean Exploration "Southern Ring of Fire expedition" in 2012, which surveyed the entire region and revealed extensive hydrothermal venting of black-smoker-type fluids at Niua South isolated to a 350 m wide and 80 m deep, steep-walled volcanic crater (Fig. 1C) at the southern flank of the volcanic edifice at 1150–1190 m water depth (Merle et al., 2012). The crater floor surrounding the hydrothermal structures is covered by fine tephra and pebble- to boulder-sized volcaniclastic pumice, pumice breccia, minor amounts of sediments, and variably oxidized sulfide talus (Fig. 2A). Clusters of inactive chimneys are found on top of the sulfide mounds, whereas the flanks are dominated by active multi-spired sulfide-sulfate chimneys (Fig. 2B). Multiple smaller accumulations of sulfide talus was found between sulfide mounds towards the northern and eastern crater rim (Fig. 1C). Inactive sulfide-sulfate chimneys (up to 10 m) and minor diffuse low-temperature venting up to 8.2 °C ("shimmering water"; Fig. 2C and D) occur on top of the sulfide mounds, whereas the active chimneys (up to 15 m) are characterized by vigorously venting of high-temperature black-smoker-type fluids from beehive diffuser and multi-spired chimney complexes on the mound flanks (Fig. 2E and F).

During R/V Sonne cruise SO263 (Haase, 2018) active (n = 3) and inactive (n = 9) sulfide-sulfate chimneys, as well as massive sulfide talus (n = 2) were recovered by TV-grab operations and ROV dives from the hydrothermal vent field of Niua South (Table 1, Fig. 1C and supplementary material 1). Fluid temperatures measured during SO263 at Niua South range from 267 to 318 °C and "vapor-flames" (Fig. 2G) indicate boiling conditions at 318 °C and ~1150 m water depth (Bischoff and Rosenbauer, 1984; Monecke et al., 2014). The sampled fluids show variable pH values (3.1–7.9) and salinities (595–695 mM Cl) slightly above seawater (540 mM Cl, Millero et al., 2008, Table 1). The active chimneys are sparsely to densely populated by white microbial mats, snails, shrimps, crabs, polychaetes, and scale worms (Fig. 2B and D). The widespread low-temperature diffuse venting (up to 8.2 °C) is restricted to the crater floor of Niua South and resulted in hydrothermal alteration and cementation of igneous rocks and sulfide talus, as revealed by local collapse pits (Fig. 2H).

3. METHODS

3.1. Bulk sulfide-sulfate analysis

Zones of seawater alteration from the outer chimney wall were removed prior to the bulk chimney investigations. Representative parts of sulfide-sulfate chimneys were crushed and milled to a grainsize of approximately 50 μm and are from here on referred to as bulk sulfides. Mineral quantities of selected samples reflecting different zones of the chimney wall (n = 10) were measured using a Siemens D5000 X-ray powder diffractometer (XRD) at the GeoZentrum Nordbayern (electronic supplement Table A2). Mineral abundances (>1 wt.%) were calculated using the Rietveld-algorithm with the Software *Profex* (Table 2) (Doebelin and Kleeberg, 2015). The results are semi-quantitative as amorphous phases were not quantified.

Element concentrations of selected bulk sulfide samples (n = 15) were measured at Activation Labs in Ontario, Canada (electronic supplement Table A2). Sample powders (0.25 g) were treated by a four-acid digest using hydrofluoric acid, followed by nitric- and perchloric acid, as well as a nitric-perchloric acid mixture. The solution was heated and evaporated to incipient dryness and afterwards redissolved using aqua regia and measured by an Agilent 735 (ICP-MS) for Mn, Ni, Mo, Ag, Cd, Bi, and Pb contents. Samples were fused with sodium peroxide and dissolved in acid for Cu and Zn measurements by ICP-OES. Instrumental neutron activation analysis (INAA) was performed to acquire Au, Ag, Ni, As, Ba, Co, Fe, Hg, Sb, Se, and Sn contents. A 30 g sample aliquot was encapsulated in a polyethylene vial and irradiated along flux wires at a thermal neutron flux of 7×10^{12} ncm^{-2} s^{-1}. After a 7-day decay-period of ^{24}Na the samples were analyzed with a high purity Ge detector with a resolution better than 1.7 KeV for the 1332 KeV Co-60 photopeak. Sulfur was oxidized in a heated oxygen environment with an accelerator material before it was measured as SO_2 in an infrared cell. Detection limits, blanks, duplicate measurements, and results of certified reference materials are listed in the electronic supplement Table A2.
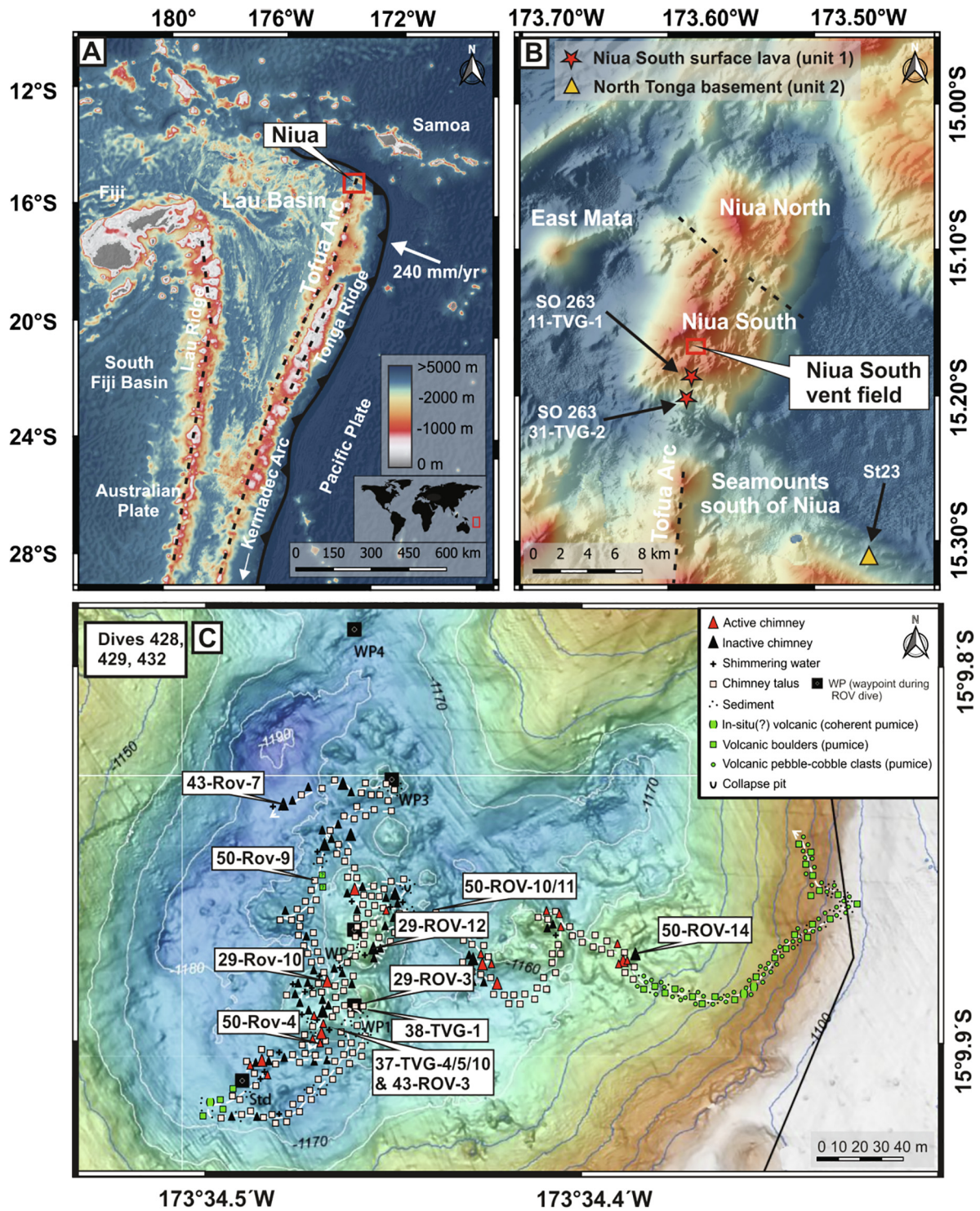
Fig. 1. (A) Bathymetric map of the Tonga arc in the western Pacific (GEBCO Bathymetric Compilation Group, 2020). (B) Bathymetric map of the working area (red rectangle) at the northern termination of the Tofua arc. The dacitic surface lavas (11-TVG-1 and 31-TVG-2) sampled during SO263 at the Niua volcanic complex are marked as red stars and the North Tonga basement basaltic andesite (St23) sampled by Falloon et al. (2007) is marked as a yellow triangle. (C) High-resolution multibeam AUV ABYSS bathymetric map of the Niua South hydrothermal field summarizing the geological observations and showing the sulfide-sulfate chimney sampling locations (Haase, 2018).
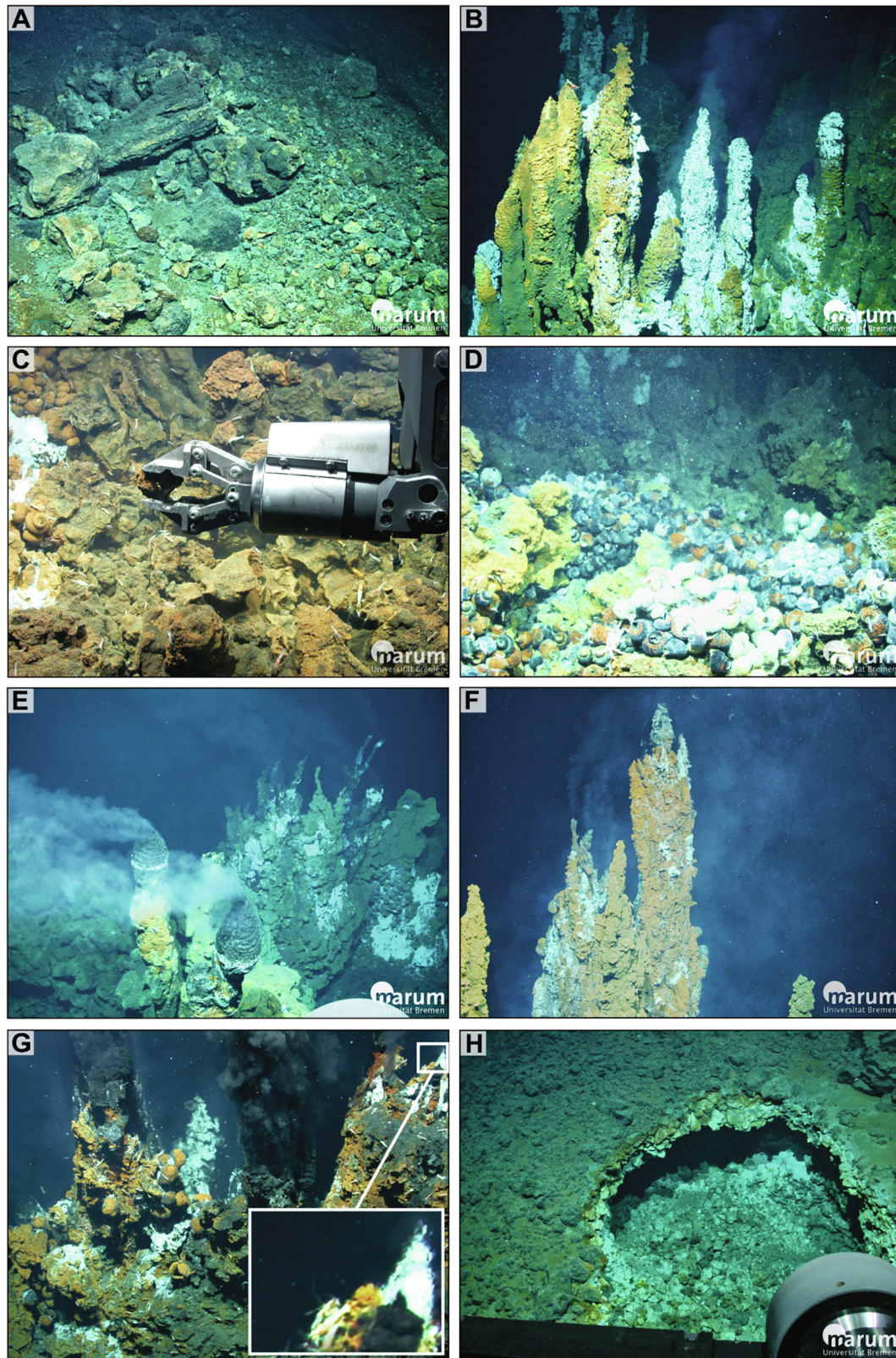
Fig. 2. Geological observations at Niua South: (A) oxidized sulfide-sulfate chimney talus, (B) sulfide-sulfate clusters of inactive and active chimney spires covered by white microbial mats (C) sampling of sulfide talus, (D) diffuse venting of "shimmering water" (E) beehive-diffuser emitting black-smoker-type fluids, (F) multi-spired chimney venting black-smoker type fluids, (G) vigorous discharge of black smoke and boiling at 318 °C (see inset with "vapor-flames"), (H) collapse pit with cementation of volcaniclastic material and sulfide-sulfate talus. (For interpretation of the references to colour in this figure legend, the reader is referred to the web version of this article.)

Table 1
Compilation of sulfide-sulfate, host rock and hydrothermal fluid samples collected during SO263 at Niua South (Haase, 2018). Chimney activity was determined visually during ROV dives and fluid samples were collected using isobaric gas-tight (IGT) fluid samplers. For more detailed information we refer to the supplementary material 1. Abbreviations: cpy = chalcopyrite, py = pyrite, sph = sphalerite, ba = barite.

Activity	Sample #	Host rock	Depth [m]	Fluid T [°C]	Cl [mM]	pH	Sample type
	29-ROV-10	Rhyolite/Dacite	1165	318	597	7.9	Cpy-py chimney
Active	43-ROV-3	Rhyolite/Dacite	1140	308–318	672	3.2–3.5	Cpy-py chimney
	50-ROV-4	Rhyolite/Dacite	1165	259–287	595–695	3.1–4.5	Sph-ba chimney
Inactive	37-TVG-4/5/10, 38-TVG-1 and 50-ROV-10/11/14	Rhyolite/Dacite	1157–1179				Cpy-py chimney
	29-ROV-12 and 43-ROV-7	Rhyolite/Dacite	1175–1177				Sph-ba chimney
Talus	29-ROV-3 and 50-ROV-9	Rhyolite/Dacite	1176–1177				Py-mrc massive sulfide

3.2. Microanalytical techniques

Polished thick sections of sulfide-sulfate chimney samples (n = 17) were petrographically examined by optical microscopy to identify the different mineral phases (Table 2). A Hitachi TM4000 tabletop scanning electron microscope (SEM) was used at the GeoZentrum Nordbayern to identify potential mineral inclusions by back-scattered electron imaging and energy dispersive X-ray spectrometry (EDS) prior to the in-situ sulfide analysis.

The major element composition (Fe, Cu, Zn, and S) of pyrite (n = 374), sphalerite (n = 209), and chalcopyrite (n = 498) in 12 samples was determined by wavelength-dispersive X-ray spectrometry (WDS) using a JEOL JXA-8200 Superprobe at the GeoZentrum Nordbayern (electronic supplement Table A3). The quantitative analysis was carried out in an evacuated chamber ($<4.3 \times 10^{-6}$ mbar) with a focused beam, an acceleration voltage of 20 kV and a beam current of 20 nA. Count times for the WDS analysis were set to 20 and 10 s for peak and background measurements, respectively. Chalcopyrite (CuK_α, FeK_α, SK_α) and sphalerite (ZnK_α) were applied as reference materials. Stoichiometric calculations were used for data quality assurance and most analyses displayed an error ≤ 3 at.% with respect to the ideal stoichiometric composition of the corresponding mineral. Each spot measured by electron probe micro analysis (EPMA) was marked on a back-scattered electron image for subsequent trace element analysis of the same mineral grain by laser ablation inductively coupled plasma mass spectrometry (LA-ICP-MS).

Trace element concentrations in pyrite (n = 170), sphalerite (n = 50), and chalcopyrite (n = 100) of selected active (n = 3) and inactive (n = 10) chimney samples were determined by a single collector quadrupole Teledyne Analyte Excite 193 nm laser coupled with an Agilent 7500c ICP–MS at the GeoZentrum Nordbayern (electronic supplement Table A3). The ICP–MS operated with a plasma power of 1190 W. Helium (0.9 l/min) and Ar (0.95 l/min) were used as carrier gases and Ar acted as plasma (14.9 l/min) and auxiliary gas (0.9 l/min). A single spot ablation pattern with a frequency of 20 Hz and a fluence of 4.04 J/cm^2 was used. Total analysis time for each spot was set to 55 s, including 20 s of gas blank analysis prior to ablation. A beam diameter of 35 to 10 μm was applied according to the size of the analyzed mineral. The following standards were used for the external calibration: Po724 B2 SRM (Au; Memorial University Newfoundland) and MASS-1 (USGS; Mn, Co, Ni, Cu, Zn, Ga, Ge, As, Se, Mo, Ag, Cd, In, Sn, Sb, Te, W, Hg, Tl, Pb, and Bi). Analytical precision was monitored by the repeated analysis of the sulfide standards yielding < 15% RSD for most elements except for Ni (18%), Cu (28%), and Hg (35%). To monitor the instrument drift the sulfide standards were analyzed several times during an analytical day (electronic supplement, Table A3). Trace element concentrations and minimum detection limits were calculated by Glitter (van Achterbergh et al., 2001) using S – analyzed by EPMA – as the internal standard. Sulfur has been chosen due to the lack of interferences in the analyzed element spectrum. There is only a $^{16}O^{18}O$ interference on ^{34}S of about 1% for all sulfides since it is produced from air (Sylvester, 2001). This is in accordance with other recently published studies that also used S for the internal standardization of sulfide analyses (Wohlgemuth-Ueberwasser et al., 2015; Keith et al., 2016, 2020).

3.3. Stable and radiogenic isotopes

Sulfur isotope measurements were performed on pyrite (n = 2), chalcopyrite (n = 3), and mixed sulfide separates (n = 5) without further chemical treatment at the Westfälische Wilhelms-Universität Münster (electronic supplement Table A4). If separation of different sulfides was not possible, mixed sulfide separates (sulfate-free inhomogeneous mixture of chalcopyrite, pyrite, and sphalerite) were used to determine the S isotope composition. About 100 μg of sulfide powder and 300–500 μm of V_2O_5 were placed into tin capsules and measured with a Flash EA IsoLink elemental analyzer interfaced to a ThermoScientific Delta V Advantage isotope ratio mass spectrometer (EA-IRMS). Reproducibility, as determined through replicate analysis of reference materials, was better than ±0.2‰ (1σ) and precision of duplicate measurement was 0.44‰ or better. Values are presented in per-mille difference relative to the Vienna-Canyon-Diablo Troilite (V-CDT) standard.

For Pb isotope measurements (n = 10) approximately 0.5 mg of sulfide powder was dissolved in 0.4 ml aqua regia

Table 2

Bulk sulfide-sulfate types and mineral abundances based on XRD and microscopic observation. The complete XRD data set is presented in the electronic supplement (Table A2) Abbreviations: T = traces (<1%), M = minor (1–5%), C = common (5–25%), A = abundant (25–50%), D = dominant (>50%), Mrc = marcasite, Py = pyrite, Cpy = chalcopyrite, Brt = barite, Sph = sphalerite, Gn = galena, Bn = bornite, Cv = covellite, Tnt-Ttr = tennantite-tetrahedrite, Cc = chalcocite, Hem = Hematite; Icb = Isocubanite; Orp = Orpiment; Au^0 = native Au; El = electrum; Bi_xTe_y = various Bi-tellurides.

Sample	Microscopic observation																XRD [wt.%]				
	Mrc	Py	Cpy	Brt	Sph	Gn	Bn	Cv	Tnt-Ttr	Icb	Cc	Orp	Hem	Au^0	El	Bi_xTe_y	Py	Cpy	Brt	Sph	Mrc
Chalcopyrite-pyrite chimneys																					
29-ROV-10		C	A	C	M	T											11	31	28	5	
43-ROV-3		T	D	T		T	T	T	T		T		T	T		T					
50-ROV-10 A		C	D	A	T							M									
50-ROV-10B		M	D	C	T																
50-ROV-14			A	A	C	M	T	T	T	T	M							42	49	2	
37-TVG-4 A	T	C	D	C	T	T	T		T			M		T	T	T	6	91	2		
37-TVG-4C	T	M	D	M	M	T						M		T		T					
37-TVG-5	T	C	D	C	C	T								T			9	62	6	12	2
37-TVG-10	T	C	D	C	C	T								T							
38-TVG-1	T	C	D	C	C	T								T		T					
Sphalerite-barite chimneys																					
29-ROV-12		M	M	D	A	T			T			M		T		T	2	2	66	29	
43-ROV-7	T	M	C	D	C	M			T			T	T				3	17	53	23	
50-ROV-4		C	C	D	C	T						T					8	6	74	11	
50-ROV-11 A		M	A	C	C		T		T					T				24	61	14	
50-ROV-11B	T	M	T	D	A	T			T			M									
Pyrite-marcasite massive sulfides																					
29-ROV-3	A	A	C	M	T												47	9	1		43
50-ROV-9	C	D	M	C	M												54	1	23	2	20

$(50/50 = 6$ M HCl/ 15 M HNO$_3$) at 80 °C in a teflon beaker (electronic supplement Table A4). After complete dissolution the solution was evaporated to dryness at 110 °C and redissolved in 1 M HCl. Lead was separated from the matrix using 100 μl Eichrom Sr-Spec resin. The sample solution was loaded onto the resin and rinsed with 1 M HCl before collecting Pb in 6 M HCl. All reagents were extra distilled and typical procedural blanks for Pb were 50 pg. Lead isotope measurements were carried out on a Thermo Fisher Scientific Neptune Plus MC-ICP-MS at the GeoZentrum Nordbayern using a ^{207}Pb/^{204}Pb double spike to correct for instrumental mass fractionation. The double spike, with a ^{207}Pb/^{204}Pb ratio of 0.82, was calibrated against a solution of the NBS982 equal atom Pb standard. Samples were diluted with 2% HNO$_3$ to a concentration of approximately 20 ppb, and an aliquot of this solution spiked in order to obtain a ^{208}Pb/^{204}Pb ratio of about one. Spiked and unspiked sample solutions were introduced into the plasma via a Cetac Aridus desolvating nebulizer and measured in static mode. Interference of ^{204}Hg on mass 204 was corrected by monitoring ^{202}Hg. An exponential fractionation correction was applied offline using the iterative method of Compston and Oversby (1969). The correction was typically 4.5‰ per amu. The NBS981 Pb isotope standard, which was measured as an unknown yielded a ^{206}Pb/^{204}Pb, ^{207}Pb/^{204}Pb, and ^{208}Pb/^{204}Pb ratio of 16.9436 ± 0.0004, 15.5011 ± 0.0004, and 36.7287 ± 0.0009, respectively. Precision of sulfide measurements for ^{206}Pb/^{204}Pb, ^{207}Pb/^{204}Pb, and ^{208}Pb/^{204}Pb were better than 0.0005, 0.0004, and 0.0010, respectively.

The trace element contents of Niua lavas (n = 2) were measured with the trace element method described previously in Storch et al. (2020) on washed rock powders using a Thermo Scientific XSERIES 2 Quadrupole ICP-MS at the GeoZentrum Nordbayern (electronic supplement Table A5). For Pb isotope double spike chemistry of the lavas, 0.10–0.12 g of the whole rock grains were leached with 6 M HCl for 1.5 h. The leaching acid was removed, and the samples were rinsed twice with MQ H$_2$O and dried overnight. The same Pb chemistry and measurement conditions were used for sulfides and lava samples. The four NBS981 standards measured with the lavas gave ^{206}Pb/^{204}Pb, ^{207}Pb/^{204}Pb, and ^{208}Pb/^{204}Pb ratios of 16.9415 ± 0.0003, 15.4990 ± 0.0002 and 36.7216 ± 0.0006, respectively. Precision of lava measurements for ^{206}Pb/^{204}Pb, ^{207}Pb/^{204}Pb, and ^{208}Pb/^{204}Pb were better than 0.0003, 0.0003 and 0.0007, respectively.

4. RESULTS

4.1. Mineralogy of the sulfide-sulfate chimneys

The chimneys show a mineralogical zoning, including a chalcopyrite-dominated lining around the central fluid conduit followed by sphalerite and barite-rich layers towards the outer chimney wall, commonly mantled by brown-orange Fe-oxides and orpiment crusts. Samples collected from the different zones were classified as chalcopyrite-pyrite and sphalerite-barite chimneys according to the prevalent mineral phases in the central and outer parts of

the chimney wall, respectively (Table 2). Sulfide talus samples that mainly consist of massive pyrite and marcasite display no mineralogical zoning and were classified as pyrite-marcasite massive sulfides (Table 2, supplementary material 1).

Pyrite, sphalerite, and chalcopyrite are assigned to different paragenetic stages of chimney growth based on variable proportions and distinct textures throughout the chimney wall (c.f. Section 5.1). Inclusion-rich pyrite framboids (py I) with growth zoning are common in the outer chimney wall, where they are surrounded and/or replaced by chalcopyrite and sphalerite (Fig. 3A and B). By contrast, euhedral pyrite occurs in the more Cu-rich inner and intermediate chimney zones, where it is either hosted by chalcopyrite (inclusion-free pristine py II, Fig. 3C and D) or forms colloform-crustiform overgrowth around chalcopyrite (inclusion-rich py III, Fig. 3E and F). Colloform textures of massive pyrite (py mas) with columnar marcasite replacement is a common feature in the talus samples (Fig. 3G). Sphalerite I forms colloform layers overprinting barite and pyrite I (Fig. 3B). Tennantite-tetrahedrite typically occurs together with sphalerite I, which locally hosts chalcopyrite and galena inclusions. Sphalerite III typically surrounds other sulfides and shows galena and native Au inclusion at the transition from chalcopyrite II to sphalerite III (Fig. 3H and O). Chalcopyrite II occurs as massive to porous colloform linings along the central conduits (Fig. 3I), whereas it occurs as disseminated grains towards the outer chimney wall (Fig. 3A). Energy dispersive X-ray spectrometry (EDS) revealed native Au, electrum (up to 45 wt.% Ag), and Bi-telluride inclusions (Bi/Te = 0.2 to 0.8) varying between < 5–10 μm in size within the chalcopyrite linings (cpy II; Fig. 3M and N). Colloform chalcopyrite II aggregates are either replaced by secondary bornite, covellite, and chalcocite or form exsolution lamellae in bornite (Fig. 3J). Dendritic intergrowths of sphalerite, chalcopyrite, bornite, and chalcocite-covellite are common textures (Fig. 3K). Barite occurs as the dominant sulfate phase (with minor amounts of anhydrite ± bassanite, CaSO$_4$ × 0.5 H$_2$O) in the outer chimney wall, and forms rosettes and dendritic intergrowth with sphalerite I (Fig. 3B) that are locally overprinted by orpiment (Fig. 3L).

4.2. Bulk chimney chemistry

Subsections from all sulfide-sulfate samples were analyzed with respect to their major, minor, and trace element composition (Table 3). Correlation coefficients (linear R^2 values) for all bivariate combinations are listed in the electronic supplement (Table A2) and are reported as strong (R^2 = 0.7–1.0), moderate (R^2 = 0.5–0.7), and weak (R^2 = 0.3–0.5). Major elements include Cu, Fe, Zn, Ba, and S, which correlate mostly with the mineralogical classification into chalcopyrite-pyrite (Cu = 1.2–24.8 wt.%), sphalerite-barite (Zn = 0.77–25.0 wt.%), and pyrite-marcasite samples (Fe = 38.4–42.2 wt.%; Tables 2 and 3). Trace element concentrations show significant variations between these groups (Fig. 4, Table 3), for example, the chalcopyrite-pyrite chimneys reach the highest Au contents, partly above the respective detection limit
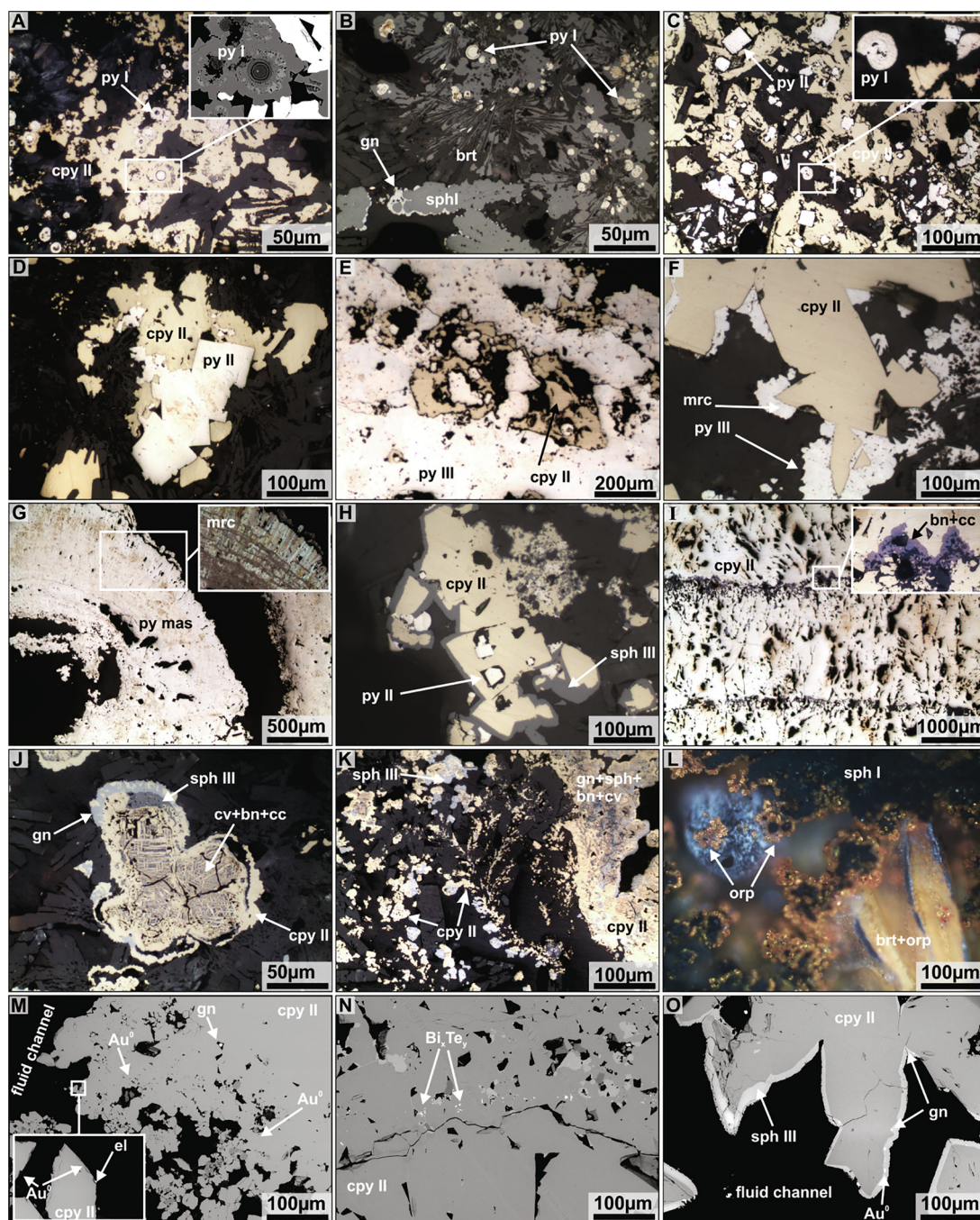
Fig. 3. Photomicrographs (A–L) and SEM images in back-scattered electron mode (M–O) of representative sulfide-sulfate samples from Niua South: (A) inclusion-rich (see BSE inset) framboidal pyrite I embedded in chalcopyrite II (50-ROV-10), (B) pyrite I framboids associated with sphalerite I together with barite dendrites and rosettes (50-ROV-11B), (C) euhedral pyrite II embedded in chalcopyrite II (29-ROV-3), (D) inclusion-free euhedral pyrite II surrounded by chalcopyrite II (50-ROV-10A). (E) massive to semi-massive pyrite III surrounding and replacing chalcopyrite II (50-ROV-10B), (F) chalcopyrite II surrounded by crustiform, inclusion-rich pyrite III and marcasite (29-ROV-10), (G) massive colloform banding of pyrite (py mas) with columnar marcasite replacement/recrystallization (29-ROV-3), (H) pyrite II and late stage inclusion-free sphalerite III surrounding chalcopyrite II (37-TVG-10), (I) massive chalcopyrite II linings replaced by bornite and chalcocite (43-ROV-3), (J) colloform chalcopyrite II aggregates with exsolution lamellae and replacement textures of covellite, chalcocite, and bornite (50-ROV-14), (K) dendritic intergrowths of chalcopyrite, sphalerite, galena, bornite, and covellite (50-ROV-14), (L) orpiment surrounding sphalerite I and overprinting barite (37-TVG-4), (M) micron-sized native Au particles in the chalcopyrite II linings (37-TVG-4), (N) Bi-telluride inclusions in chalcopyrite II (43-ROV-3), (O) native Au and galena inclusion in sphalerite III surrounding chalcopyrite II (37-TVG-4). Abbreviations: bn = bornite, brt = barite, cc = chalcocite, cv = covellite, cpy = chalcopyrite, gn = galena, mrc = marcasite, orp = orpiment, py = pyrite, sph = sphalerite, el = electrum. (For interpretation of the references to colour in this figure legend, the reader is referred to the web version of this article.)

Table 3
Compilation of bulk sulfide-sulfate data from Niua South, mid-ocean ridges (Fouquet et al., 1998; Hannington and Scott, 1988, Rona et al., 1993; Grant et al., 2018; Monecke et al. 2016; Hekinian et al., 1980; Auclair et al., 1987; Münch et al., 1999; Hannington et al., 2005; Kristall et al., 2006; Pašava et al., 2007; Melekestseva et al., 2014; Webber et al., 2015; Wang et al., 2017) and Brothers volcano (de Ronde et al., 2011). The complete Niua South data set is presented in the electronic supplement (Table A2). Abbreviations: G.M. = geometric mean, G.SD. = geometric standard deviation.

| Bulk sulfide-sulfates		S	Fe	Cu	Zn	Ba	Mn	Co	Ni	As	Se	Mo	Ag	Cd	Sb	Au	Pb	Bi
		wt.%					ppm											
Cpy-py	Min.	21.7	7.54	1.91	0.470	0.650	10.0	1.00	1.00	1100	1.50	11.0	53.4	11.5	122	6.39	354	1.00
(n = 8)	Max.	33.8	24.9	24.8	15.2	32.7	206	265	1.00	10,000	70.0	436	510	365	1400	>30.0	5000	15.0
	G.M.	27.6	15.4	10.4	4.47	8.85	55.4	97.7	1.00	3659	3.64	77.2	218	117	592	18.4	1653	4.21
	G.SD.	1.18	1.59	2.38	3.46	4.52	2.71	6.45	1.00	2.04	5.21	3.80	2.02	3.20	2.31	1.76	2.60	2.72
Sph-brt	Min.	20.4	2.20	0.260	0.770	26.0	30.0	24.0	1.00	486	1.50	7.00	176	55.2	294	3.23	232	1.00
(n = 5)	Max.	24.9	12.4	13.2	25.0	39.9	47.0	151	3.00	6310	1.50	117	741	1160	1580	>30.0	5000	4.00
	G.M.	22.1	4.96	2.08	8.99	33.4	38.9	54.0	1.25	2294	1.50	23.7	385	384	809	10.0	1348	1.32
	G.SD.	1.08	2.09	4.73	4.26	1.20	1.19	1.99	1.63	2.64	1.00	3.26	2.01	3.63	2.14	2.26	3.40	1.86
Py-mrc	Min.	48.4	38.4	0.250	0.14	0.700	255	26.0	6.00	3780	1.50	65.0	18.3	4.30	30.8	3.05	86.0	5.00
(n = 2)	Max.	49.1	42.2	4.28	0.80	7.42	562	206	7.00	5230	84.0	90.0	34.6	24.8	59.4	3.70	268	19.0
	G.M.	48.8	40.3	1.04	0.33	2.28	379	73.2	6.48	4446	11.2	76.5	25.2	10.3	42.8	3.36	152	9.75
	G.SD.	1.01	1.07	7.39	3.43	5.31	1.75	4.32	1.12	1.26	17.2	1.26	1.57	3.45	1.59	1.15	2.23	2.57
MOR	Min.	0.100	0.100	0.010	0.010	0.001	5.27	0.600	0.153	2.00	1.10	0.100	0.500	0.430	0.060	0.01	0.001	0.010
Sulfides	Max.	53.9	58.1	56.2	49.7	27.5	6550	6100	600	23,000	1505	598	1788	2820	3503	471	74,000	79.0
(n = 392)	G.M.	36.3	29.5	7.12	6.26	0.840	545	370	37.0	301	118	71.0	91.7	209	47.5	7.66	1038	7.04
	G.SD.	11.2	12.8	11.0	10.1	3.03	902	753	69.6	1415	212	72.6	180	366	252	33.1	4755	12.3
Brothers	Min.	0.330	2.08	0.002	0.002	0.004	15.5	2.00	1.00	2.30	6.00	2.00	0.700	0.500	0.840	0.02	8.00	0.500
Sulfides	Max.	57.7	50.2	35.6	43.8	48.4	1727	850	23.0	14,200	1690	910	1420	4140	1690	91.4	18,800	1490
(n = 56)	G.M.	24.8	13.0	0.914	0.847	5.35	89.9	25.4	3.13	1274	117	57.9	47.1	62.1	82.8	2.82	513	11.3
	G.SD.	2.58	1.90	13.6	11.8	8.41	4.94	4.72	1.91	4.88	4.72	4.42	4.00	10.6	4.39	5.13	5.99	10.8
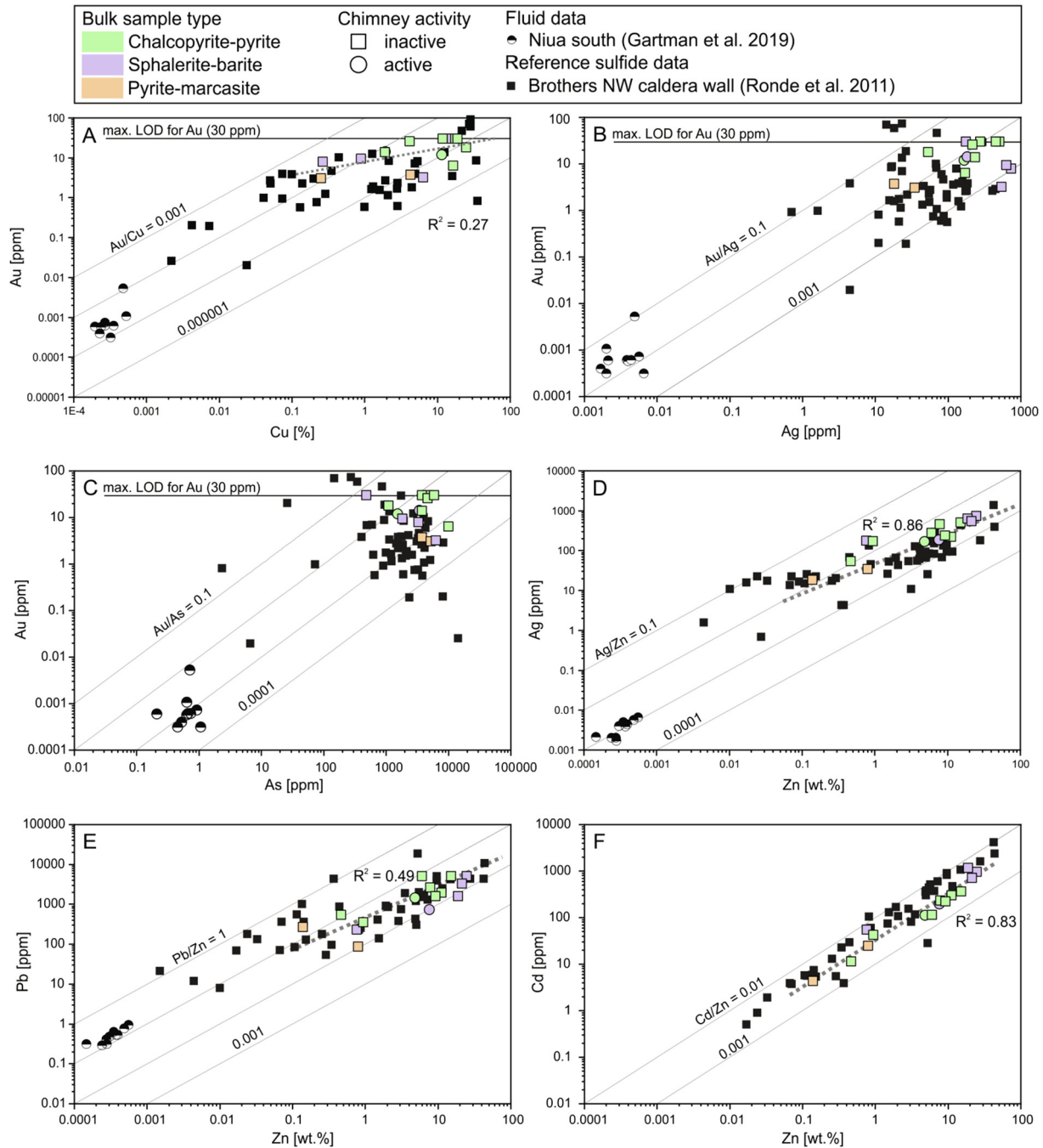
Fig. 4. Bivariate variation diagrams of chalcopyrite-pyrite and sphalerite-barite chimneys as well as pyrite-marcasite massive sulfide samples from Niua South in comparison with hydrothermal fluid data from Niua South (Gartman et al., 2019) and bulk sulfide data from Brothers volcano (de Ronde et al., 2011). Note that the correlation coefficients (R^2 values) are listed in the electronic supplement (Table A2). Black lines in (A-C) represent maximum detection limits for Au and several measurements above 30 ppm Au are reported as 30 ppm and, thus, represent minimum values. (For interpretation of the references to colour in this figure legend, the reader is referred to the web version of this article.)

(>30 ppm), and thus are reported as 30 ppm representing minimum values. Furthermore, they show high concentrations of Co, As, and Mo, whereas sphalerite-barite samples have high Ag, Cd, Sb, Ba, and Pb contents (Table 3). By contrast, the pyrite-marcasite samples are depleted in most trace elements except Mn, Ni, Se, and Bi. Weak to strong correlations have been observed in

bivariate combinations of Au-Cu ($R^2 = 0.27$), Ag-Zn ($R^2 = 0.86$), Pb-Zn ($R^2 = 0.49$), and Zn-Cd ($R^2 = 0.83$) (Fig. 4A, D, E, and F). Selenium/S*10^6 ratios in two chalcopyrite-pyrite and one pyrite-marcasite sample, where Se is above the respective detection limit (>3ppm), range from 128 to 235 with a mean of 176 (supplementary material 1).

The chemical composition of the Niua South bulk sulfides is comparable to those from Brothers volcano (Figs. 4 and 5), which are both depleted in Mn, Fe, Co, Ni, and Se and enriched in Au, As, and Sb compared to mean mid-ocean ridge bulk sulfides (Fig. 5). The hydrothermal fluids from Niua South (Gartman et al., 2019) are enriched in Mn, Fe, and Cu and depleted in Zn, Ba, and Pb compared to the dacitic host rocks (Fig. 5), and show element ratios (e.g., Au/Cu, Au/Ag, Ag/Zn) broadly comparable to the bulk sulfide composition of Niua South (Fig. 4).

4.3. Mineral chemistry

Pyrite is the main host for Co, Ni, Tl, Mo, and Te and chalcopyrite for Sn, Bi, In, and Se, while sphalerite typically shows intermediate trace element contents except for Sb and Cd (not shown), with respect to the median or mean values (Fig. 6). Correlation coefficients (linear R^2 values) for all bivariate trace element combinations in pyrite, sphalerite, and chalcopyrite are presented in the electronic supplement (Table A3) and are reported as strong ($R^2 = 0.7$–1.0), moderate ($R^2 = 0.5$–0.7) and weak ($R^2 = 0.3$–0.5).

Iron, Cu, and S in pyrite vary from 41.6 to 48.0, 0.05 to 5.0, and 48.1 to 54.4 wt.%, respectively. The trace element composition of the different pyrite types is distinct (c.f. Section 4.1), as reflected by a Cu, Zn, Mo, Au, and Tl enrichment and Co, Se, Cd, Sn, and Te depletion in pyrite I compared to pyrite II and III (Table 4 and Fig. 6). By contrast, pyrite II is characterized by high Se and Sn, as well as low Ni and Mo compared to pyrite I and III. Pyrite III displays elevated concentrations in Co and Te compared to pyrite I and II. Cobalt and Te concentrations increase, whereas Tl contents decrease from pyrite I to pyrite III (Fig. 6). Silver, Sb, Te, Au, and Pb in pyrite plot on the As-rich end of the wedge-shaped compositional zone defined by mid-ocean ridge, back-arc, and island arc

hydrothermal pyrite (Fig. 7A–E, Keith et al., 2016). Thallium shows a similar wedge-shaped compositional variation with As in pyrite (Fig. 7F, Deditius and Reich, 2016). Selenium/Tl and Co/Ni ratios are lower in pyrite I compared to pyrite II and III and exhibit a moderately positive correlation ($R^2 = 0.68$) (Fig. 7G). Furthermore, pyrite III (±II) shows lower Sb/Pb, Bi/Pb, and Tl/Pb ratios compared to pyrite I and massive pyrite (py mas), and overlap with hydrothermal pyrite sampled from the boiling zone of the Cerro Pabellón geothermal systems (Fig. 7H and I) (Román et al., 2019). Selenium/S*10^6 ratios in all pyrite types typically range from 0.6 to 1470 with a mean of 94.8 (supplementary material 1). Trace element ratios of Au/As, Te/As, and Ag/As of euhedral pyrite II and III are mostly comparable to the hydrothermal fluids, although absolute concentrations are much lower in the fluids (Fig. 7A–C). Arsenic and Sb concentrations in pyrite from Niua South (2.6 ppm to 2.4 wt.% As and 0.034 ppm to 0.32 wt.% Sb) are comparable to those from other submarine arc-related hydrothermal systems like Brothers volcano and Volcano 19 (1.3 ppm to 2.0 wt.% As; 0.028 ppm to 0.086 wt.% Sb) but show a distinct enrichment compared to pyrite from back-arc (0.4 ppm to 0.4 wt.% As; 0.027 ppm to 0.024 wt.% Sb), and mid-ocean ridge hydrothermal systems (0.1 ppm to 0.5 wt.% As; 0.021 ppm to 0.031 wt.% Sb, Fig. 7E).

Zinc, Fe, Cu, and S in sphalerite vary from 42.2 to 65.6, 0.20 to 11.2, 0.05 to 10.4, and 30.6 to 34.1 wt.%, respectively. Within the sphalerite subgroups (c.f. Section 4.1), sphalerite I is enriched in Ge, As, Ag, Cd, Hg, Tl, and Pb compared to sphalerite III, which displays elevated concentrations in Mn, Fe, Co, Ni, Ga, Se, Mo, In, Sn, Te, Au, and Bi (Table 4, Fig. 6). Iron and Zn show a moderately negative correlation ($R^2 = 0.66$) following a well-established trend similar to sphalerite from other submarine hydrothermal systems (Fig. 8A, Keith et al., 2014.) Gallium/Ge and
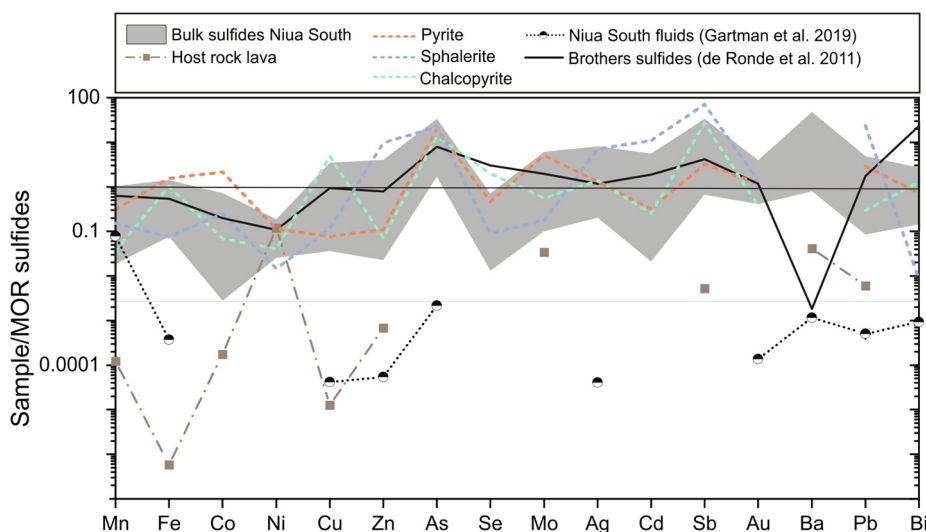

Fig. 5. Multi-element diagram showing the bulk sulfide-sulfate samples, the dacitic host rocks (electronic supplement Table A5), the hydrothermal fluids (Gartman et al., 2019) as well as in-situ pyrite, chalcopyrite, and sphalerite composition from Niua South normalized to mean mid-ocean ridge bulk sulfides (c.f. Table 2). Brothers sulfides reference data is from de Ronde et al. (2011). (For interpretation of the references to colour in this figure legend, the reader is referred to the web version of this article.)
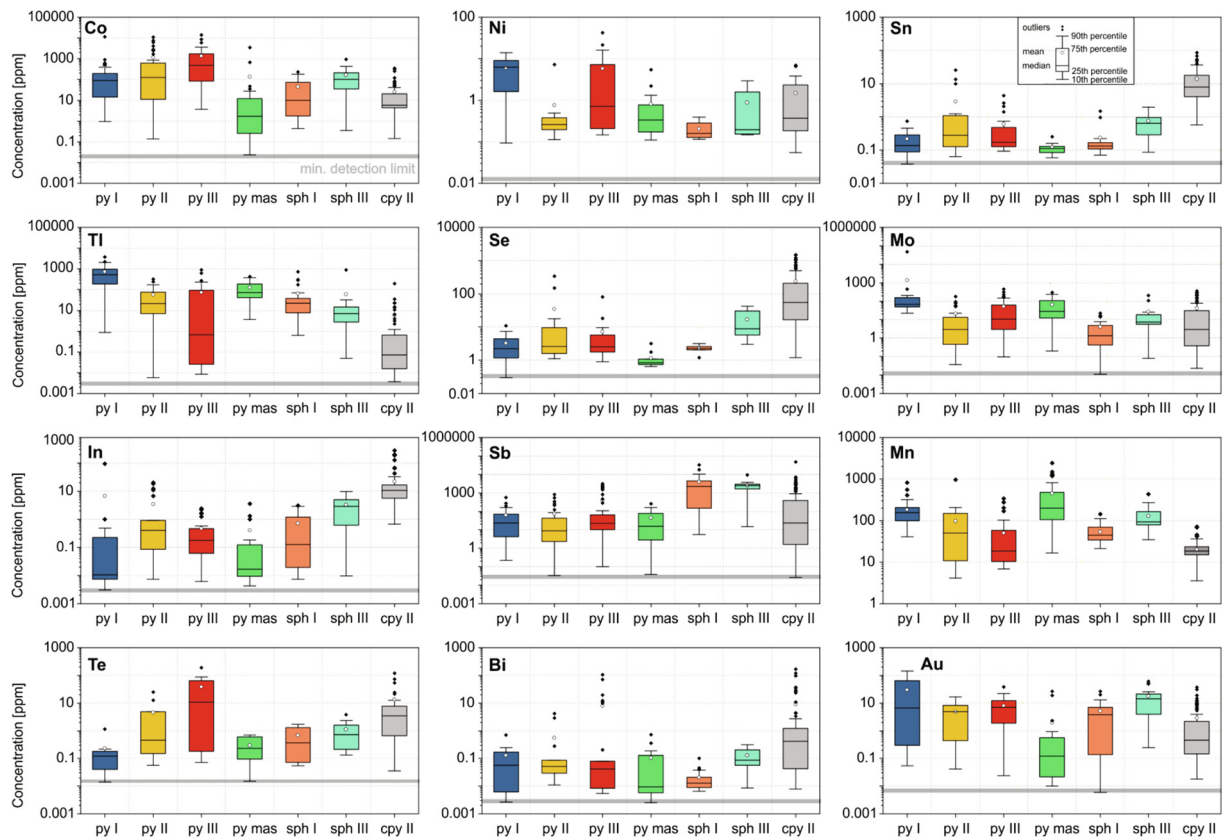
Fig. 6. Box and whisker plots of selected trace elements in pyrite, sphalerite, and chalcopyrite analyzed by LA-ICP-MS with respect to their paragenetic evolution (c.f. Table 5 and Section 5.1). The grey lines define the minimum detection limits of the respective element. Mean values (white dots) are calculated based on the entire dataset (including outliers), and thus might plot outside the respective box, whereas median values are based solely on data within the box (25th to 75th percentile). (For interpretation of the references to colour in this figure legend, the reader is referred to the web version of this article.)

Fe/Zn ratios systematically increase from sphalerite I to sphalerite III and display a moderately positive correlation ($R^2 = 0.43$) (Fig. 8B).

Chalcopyrite has a near stoichiometric composition and is depleted in most trace elements compared to the other sulfides, except for Se, In, Sn, Te, and Bi (Table 4, Fig. 6). Zinc and Cd correlate moderately positive ($R^2 = 0.59$, not shown) in chalcopyrite and show low Cd/Zn ratios (G.M. Cd/Zn = 0.007).

4.4. Sulfur and Pb isotopes

The Niua South sulfides range in $\delta^{34}S$ composition from −0.3 to 4.4‰ (electronic supplement Table A4) and overlap with values from sediment-free MOR hydrothermal systems that are described by a $\delta^{34}S$ composition between mid-ocean ridge basalt (−0.9 ± 0.5‰, Labidi et al., 2012, 2014) and seawater (21.2 ± 0.9‰, Tostevin et al., 2014). Furthermore, the $\delta^{34}S$ composition of the Niua South sulfides overlaps with those of the associated hydrothermal vent fluids (2.6–3.6‰, Gartman et al., 2019), volcanic glass samples from nearby (<10 km) Mata volcano (−0.2 to 2.0‰, Keller et al., 2009), and global island arc volcanic rocks (5.0 ± 3.9‰, Ueda and Sakai, 1984; Woodhead

et al., 1987; Alt et al., 1993; Hoog et al., 2001). Pyrite shows the lowest (−0.3 to 1.0‰), chalcopyrite intermediate (1.7–1.8‰), and mixed sulfide separates the highest $\delta^{34}S$ values (3.6–4.4‰; Fig. 9). Sulfide separates from active vents show similar $\delta^{34}S$ signatures (1.8–4.0‰) like those from inactive vents (−0.3 to 4.4‰).

The Pb isotope composition of the Niua South hydrothermal sulfides ranges from 18.857 to 18.866, 16.621 to 16.626, and 38.832 to 38.845 for $^{206}Pb/^{204}Pb$, $^{207}Pb/^{204}Pb$, and $^{208}Pb/^{204}Pb$, respectively, exhibiting a $^{206}Pb/^{204}Pb$ signature comparable to that of other north Tonga lavas (Fig. 10) (Regelous et al., 1997; Wendt et al., 1997; Ewart et al., 1998; Falloon et al., 2007). By contrast, the $^{207}Pb/^{204}Pb$ and $^{208}Pb/^{204}Pb$ ratios of hydrothermal sulfides and dacitic lavas from Niua South are higher than those of the other north Tonga lavas (Fig. 10, electronic supplement Table A5). The $^{206}Pb/^{204}Pb$, $^{207}Pb/^{204}Pb$, and $^{208}Pb/^{204}Pb$ signatures of the Niua South hydrothermal sulfides are also systematically lower than those of the dacitic host rock lavas and display a trend towards the Pb isotope composition of the older Tonga basement basaltic andesites (sample St23 measured by Falloon et al., 2007, Fig. 1B). No systematic difference between active and inactive samples occur with respect to their Pb isotope composition (Fig. 10).

Table 4

Compilation of in-situ pyrite, sphalerite, and chalcopyrite trace element data with respect to the paragenetic relations (c.f. Table 5). The complete data set is presented in the electronic supplement (Table A3). Abbreviations: G.M. = geometric mean, G.SD. = geometric standard deviation.

| Minerals		Fe	Cu	Zn	Mn	Co	Ni	Ga	Ge	As	Se	Mo	Ag	Cd	In	Sn	Sb	Te	Au	Hg	Tl	Pb	Bi
		EPMA [wt.%]			LA-ICP-MS [ppm]																		
Pyrite I	Min.	41.2	0.050	0.040	41.0	0.950	0.090	0.010	0.530	2458	0.300	22.43	0.030	0.170	0.000	0.040	0.220	0.010	0.010	0.120	0.880	7.02	0.000
n = 40	Max.	47.4	5.00	4.59	818	1135	14.0	6.96	9.35	23,554	10.9	46,819	2881	96.0	93.0	0.740	560	1.16	336	2.42	3734	61,915	0.710
	G.M.	44.9	0.500	0.450	149	55.2	3.58	0.360	2.17	6491	2.21	96.9	23.0	2.85	0.050	0.150	16.1	0.100	3.44	0.59	384	988	0.040
	G.SD.	1.03	3.08	3.31	1.89	7.86	3.96	5.62	1.85	1.72	2.69	3.43	32.8	4.61	16.8	2.41	7.25	3.99	30.6	2.48	4.28	9.25	6.61
Pyrite II	Min.	45.9	0.050	0.040	4.11	0.140	0.110	0.020	0.320	2.55	1.10	0.040	0.040	0.130	0.010	0.06	0.030	0.060	0.040	0.080	0.010	0.820	0.010
n = 46	Max.	48.0	1.04	0.960	959	11,008	15.4	89.8	44.2	12,489	780	179	188	355	20.0	25.3	825	109	16.8	116	323	5355	48.1
	G.M.	46.9	0.240	0.11	40.2	106	0.750	1.03	2.73	1959	18.9	4.15	4.26	4.01	0.570	0.64	6.98	2.64	2.15	0.36	5.24	50.4	0.530
	G.SD.	1.01	2.35	2.57	3.60	11.0	5.10	8.53	3.14	4.99	11.7	7.59	5.64	7.76	8.93	5.80	10.3	9.26	4.42	5.66	23.5	7.60	20.0
Pyrite III	Min.	44.3	0.060	0.070	6.88	3.63	0.150	0.020	0.460	626	0.900	0.100	0.080	0.060	0.010	0.090	0.100	0.070	0.020	0.130	0.010	0.81	0.010
n = 51	Max.	47.5	2.32	1.42	338	14,108	42.3	389	152	17,499	80.7	453	3441	2049	2.38	4.32	3177	189	38.5	49.8	883	63,330	105
	G.M.	46.2	0.27	0.43	26.2	344	1.21	1.04	2.04	6491	3.32	12.4	7.17	11.0	0.150	0.28	32.9	3.08	3.39	2.17	1.51	280	0.090
	G.SD.	1.02	2.79	2.69	2.95	7.40	6.49	13.3	4.61	2.05	2.82	7.29	7.84	14.8	5.40	3.03	10.3	22.6	6.16	9.25	53.8	17.9	21.5
Pyrite mas	Min.	46.4	0.060	0.060	16.7	0.020	0.110	0.010	0.470	726	0.650	0.200	0.020	0.030	0.000	0.060	0.040	0.020	0.010	0.110	3.63	0.250	0.000
n = 33	Max.	47.8	0.230	0.060	2406	3497	5.42	9.95	3.16	16,002	3.19	292	45.5	77.7	3.60	0.250	259	0.710	26.5	1.07	421	1748	0.720
	G.M.	47.1	0.100	0.060	239	2.14	0.440	0.130	1.68	3251	1.02	21.02	2.10	0.67	0.040	0.110	12.4	0.180	0.140	0.29	74.3	46.6	0.020
	G.SD.	1.01	1.65	1.00	3.21	16.2	2.87	5.58	1.69	2.20	1.64	7.32	9.78	4.74	8.41	1.47	8.56	3.36	8.05	1.90	3.12	8.27	6.23
Sphalerite I	Min.	0.150	0.050	42.2	21.3	0.440	0.120	0.040	10.8	218	1.21	0.010	14.2	755	0.010	0.070	5.71	0.060	0.010	2.47	0.620	1296	0.010
n = 31	Max.	9.20	10.4	65.6	143	235	0.390	506	362	81,221	3.20	22.1	4308	12,085	3.08	1.47	32,912	1.72	26.9	272	723	694,217	0.100
	G.M.	0.860	0.420	62.7	48.6	10.0	0.180	34.7	68.4	3806	2.17	1.31	403	1804	0.130	0.160	1023	0.370	1.26	50.1	17.8	10,342	0.020
	G.SD.	1.90	2.79	1.04	1.58	8.34	1.71	11.3	2.53	3.87	1.39	6.41	4.34	1.84	8.29	2.10	9.19	3.76	10.9	2.44	4.96	3.10	2.01
Sphalerite III	Min.	0.970	0.070	53.8	34.8	0.360	0.150	14.1	1.26	2.66	3.02	0.080	37.3	395	0.010	0.090	15.0	0.130	0.250	6.31	0.050	24.3	0.010
n = 19	Max.	11.2	3.67	64.0	435	918	2.96	2043	97.8	9902	42.9	203	1210	6430	9.77	1.99	9361	3.79	60.4	85.0	908	30,347	0.320
	G.M.	3.36	0.690	59.4	108	67.2	0.36	219	36.3	872	11.6	7.49	227	1477	1.10	0.510	1477	0.620	9.12	22.2	6.93	4607	0.090
	G.SD.	2.10	2.23	1.05	1.80	7.34	4.16	3.85	2.55	8.34	2.62	6.28	2.52	2.26	9.19	2.69	4.59	3.39	4.40	1.90	6.89	7.14	2.88
Chalcopyrite II	Min.	27.4	30.3	0.040	3.54	0.140	0.060	0.270	0.400	0.500	1.19	0.02	0.510	0.180	0.670	0.570	0.030	0.040	0.020	0.100	0.000	0.030	0.010
n = 100	Max.	31.6	35.6	1.59	71.6	354	6.96	457	107	224,177	1498	358	1461	1205	280	85.8	48,027	121	37.2	28.7	199	5967	170
	G.M.	30.4	34.6	0.24	17.6	8.11	0.530	8.10	4.74	58.5	63.3	3.49	52.8	2.03	9.61	8.20	27.1	2.60	0.590	1.48	0.140	14.5	0.370
	G.SD.	1.01	1.01	3.51	1.71	4.64	4.47	5.98	3.54	23.0	6.00	13.2	5.50	7.41	3.25	2.94	29.8	7.51	6.50	4.26	14.7	21.7	13.7
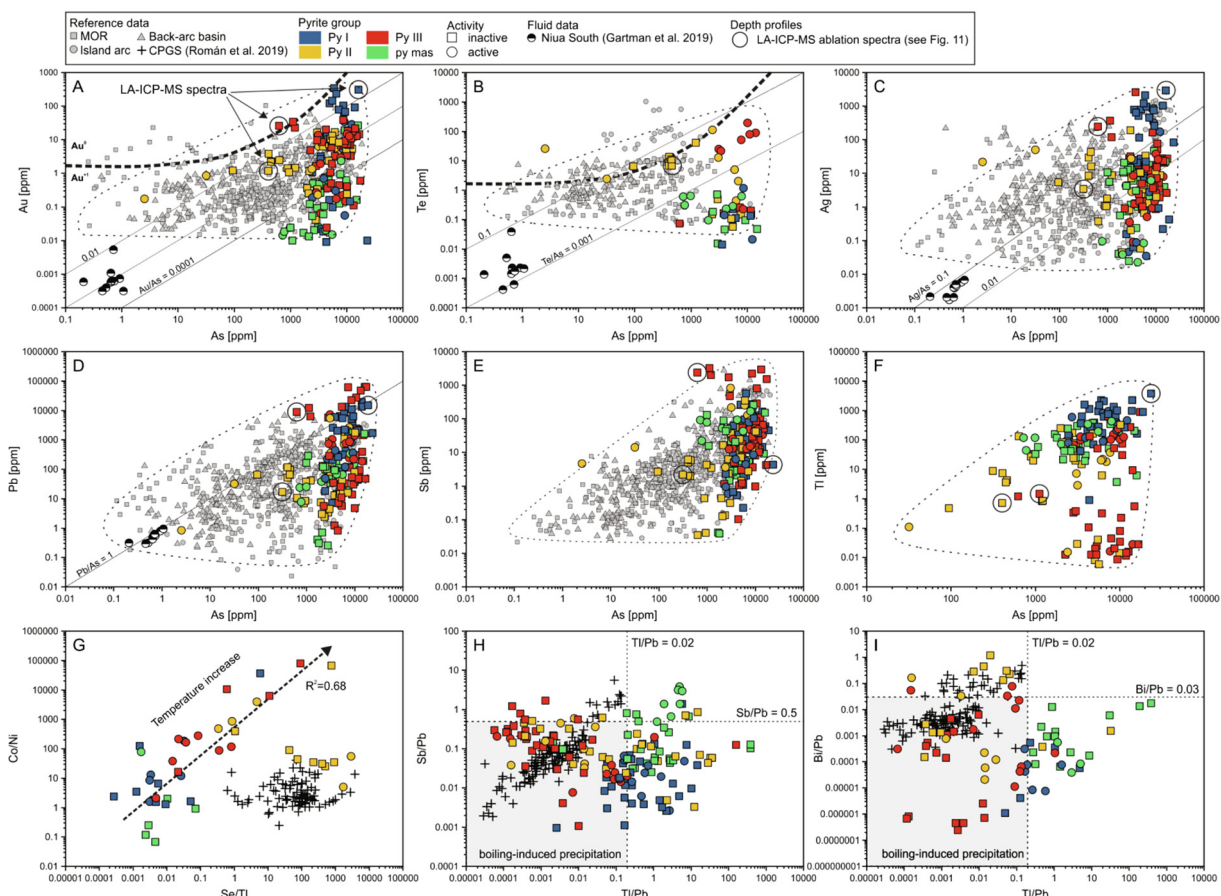
Fig. 7. Bivariate variation diagrams of selected trace elements vs. As (A–F) and ratio-ratio plots (G–I) in pyrite from Niua South. The wedge-shaped compositional zones of trace elements vs. As (A–F) are defined by the grey dashed line based on the compositional variety of submarine hydrothermal pyrite from Keith et al. (2016). The black dashed lines in (A) and (B) represent the solubility limit of Au and Te as a function of As in pyrite (Reich et al., 2005; Keith et al., 2018a). Representative time-integrated LA-ICP-MS depth profiles of pyrite I, II and III (black circles in A–F) are presented in Fig. 11B–D. The paragenetic relationship of pyrite I to III is presented in Table 5 and described in Section 5.1. Reference data for pyrite after Wohlgemuth-Ueberwasser et al. (2015), Keith et al. (2016), and Román et al. (2019) and hydrothermal fluid data from Niua South is from Gartman et al. (2019). The compositional fields for "boiling-induced precipitation" are defined by low Sb/Pb (<0.5), Tl/Pb (<0.03) and Bi/Pb (<0.02) ratios in pyrites and are redrawn after Román et al. (2019). Abbreviations: CPGS = Cerro Pabellón Geothermal System. (For interpretation of the references to colour in this figure legend, the reader is referred to the web version of this article.)

5. DISCUSSION

5.1. Sulfide-sulfate precipitation and chimney maturation

Mixing between hydrothermal fluids and seawater is the primary process driving mineral precipitation during the initial stage of chimney growth (stage 1). This is reflected by the early precipitation of barite (and anhydrite) rosettes (Fig. 3B, Table 5; Haymon, 1983; Tivey et al., 1999; Berkenbosch et al., 2012). These early sulfates formed an immature barrier between the hydrothermal fluid and ambient seawater, and acted as nuclei for subsequent low-temperature sulfide precipitation including sphalerite (Fig. 3B) and framboidal pyrite (Fig. 3A and B) (Berkenbosch et al., 2012). Early anhedral sulfides typically formed by rapid precipitation and quenching of H_2S-rich fluids induced by strong undercooling at temperatures <150–200 °C, as revealed by their dendritic textures in the

outer chimney zones (Fig. 3B) (Murowchick and Barnes, 1987; Xu and Scott, 2005; Maslennikov et al., 2009; Berkenbosch et al., 2012; Gartman and Luther III, 2013). Similarly, As-rich low-temperature fluids (<100 °C) were likely involved in the early stage of chimney growth, as indicated by orpiment precipitation on the outer chimney wall (Table 5; Dekov et al., 2013). The formation of pristine euhedral pyrite (py II) (>250 °C; Murowchick and Barnes, 1987) and chalcopyrite II (300–350 °C; Metz and Trefry, 2000) reflects the onset of a more stable hydrothermal environment during the high-temperature stage 2 (Fig. 3A, C, D, and F, Table 5). This change in morphology and mineralogy from stage 1 to stage 2 (Table 5) reflects the evolution from a young low-temperature (<250 °C) seawater-dominated to a more mature system with a steady and high temperature (up to 325 °C) fluid flux and less seawater mixing (Haymon, 1983; Tivey et al., 1999; Berkenbosch et al., 2012; Wohlgemuth-Ueberwasser et al.,
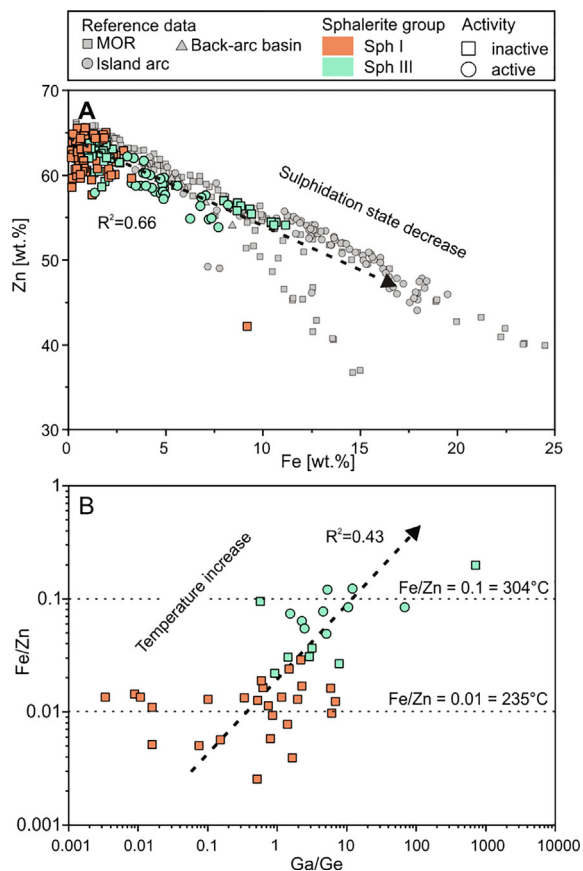
Fig. 8. Bivariate variations diagrams of (A) EPMA major element data of Zn vs. Fe and (B) combination of EPMA Fe/Zn vs. LA-ICP-MS Ga/Ge ratios in sphalerite from Niua South. The paragenetic relationship of sphalerite I and III is presented in Table 5 and described in Section 5.1. Reference data and temperature calculation after Keith et al. (2014). (For interpretation of the references to colour in this figure legend, the reader is referred to the web version of this article.)

2015; Gartman et al., 2018). Dendrites of chalcopyrite and sphalerite (Fig. 3K) indicate co-precipitation of Cu and Zn (stage 3A, Table 5), which disagrees with fluid–solid equilibrium during simple seawater mixing, since Cu precipitation commonly starts at >300 °C, whereas sphalerite does not precipitate until temperatures are <200–250 °C (Metz and Trefry, 2000; Klevenz et al., 2011; Keith et al., 2021). Fluid boiling induced destabilization of metal complexes may have led to a co-precipitation of phases that would typically form under distinct conditions like chalcopyrite and sphalerite (Ueno et al., 2003; Pokrovski et al., 2014; Keith et al., 2016). Colloform and crustiform textures of inclusion-rich pyrite III (mature stage 3A) can be linked to rapid crystallization and supersaturation of metal and semi-metals in hydrothermal fluids, which could also be related to fluid boiling (Román et al., 2019). Therefore, the occurrence of pyrite III may define the onset of the boiling stage at Niua South (Table 5), which can be separated into a high temperature vapor-dominated stage 3A and an intermediate temperature liquid-dominated stage 3B (c. f. Section 5.4; Table 5). These two stages are preserved by

crustiform inclusion-rich pyrite III postdating chalcopyrite II (stage 3A, Fig. 3F), as well as late-stage sphalerite III (stage 3B, Fig. 3H). The replacement and recrystallization of massive colloform pyrite to columnar shaped marcasite in inactive samples (Fig. 3G) likely represent a low-temperature (100 to 250 °C) overprint and dissolution- and reprecipitation processes based on zone refining (Fouquet et al., 1998; Berkenbosch et al., 2012; Grant et al., 2018). The intimate association of co- and post genetic native Au, electrum, Bi-telluride particles, chalcopyrite II, and sphalerite III (Fig. 3M–O) suggest a formation and incorporation during stage 3A subsequent to the boiling stage (stage 3B; Table 5). This can be explained by drastic and abrupt boiling-induced changes in fluid conditions like decreasing fS_2 and temperature, as well as increasing fO_2 and pH causing metal complex destabilization and precipitation (Drummond and Ohmoto, 1985; Cooke and McPhail, 2001; Ciobanu et al., 2006; Gartman et al., 2018). For instance, fS_2 and fO_2 in hydrothermal systems are controlled by the quantities of dissolved H_2 and H_2S in the fluids (Kawasumi and Chiba, 2017). Near-boiling vent fluids analyzed from unsedimented back-arc hydrothermal systems reveal variable H_2S (order of magnitude of 10) and fairly low but uniform H_2 contents (Reeves et al., 2011). The equilibrium reaction $H_2O_{(l)} + S_{2(g)} = H_2S_{(aq)} + O_{2(g)}$ indicates that Log fS_2 of a hydrothermal solution with unit water activity is given by Log fO_2 + 2*(log a $H_2S_{(aq)}$ + log K). Hence, if fO_2 (set by $aH_{2(aq)}$) is constant, fS_2 should drop by two log units when the H_2S content of the fluid decreases by one log unit inducing, for example, the formation of native Au. Ratios of Bi/Te are variable (0.19 to 0.77), but mostly resemble tellurobismuthite (Bi_2Te_3), which was also identified as colloids in liquid-dominated fluids at Niua South (Gartman et al., 2019), and its formation may also be related to boiling-induced drastic changes in fluid fS_2 (Cooke and McPhail, 2001; Ciobanu et al., 2006). This accumulation of boiling-induced mineral particles in the mature stage of chimney growth likely reflects the upwelling of phase separated liquid-dominated fluids (stage 3B) transporting these particles (c.f. Section 5.4) in lower tempered fluids (Gartman et al., 2018, 2019), as reflected by the stability of sphalerite relative to chalcopyrite in the mature stage 3B (Metz and Trefry, 2000).

5.2. Trace metal incorporation in pyrite, chalcopyrite, and sphalerite

Trace elements are hosted in sulfides either in solid solution or as micro- to nanoscale inclusions (Reich et al., 2005; Deditius et al., 2014; Deditius and Reich, 2016; Keith et al., 2018). Solid solution incorporation is mainly controlled by the physical- and chemical properties of the crystal lattice, such as the crystal symmetry, covalent radii, and formal charges (Abraitis et al., 2004; Reich et al., 2005; Keith et al., 2018). Three types of incorporation mechanisms are distinguished for pyrite, including (1) elements that often form inclusions (Cu, Zn, Ag, Sb, Pb, Bi ± Au ± Te), (2) elements that occur in solid solution due to non-stoichiometric substitution (Mo, Au, Tl), and (3) stoichiometric substitution (As, Co, Ni, Se) (Abraitis et al., 2004; Reich et al.,
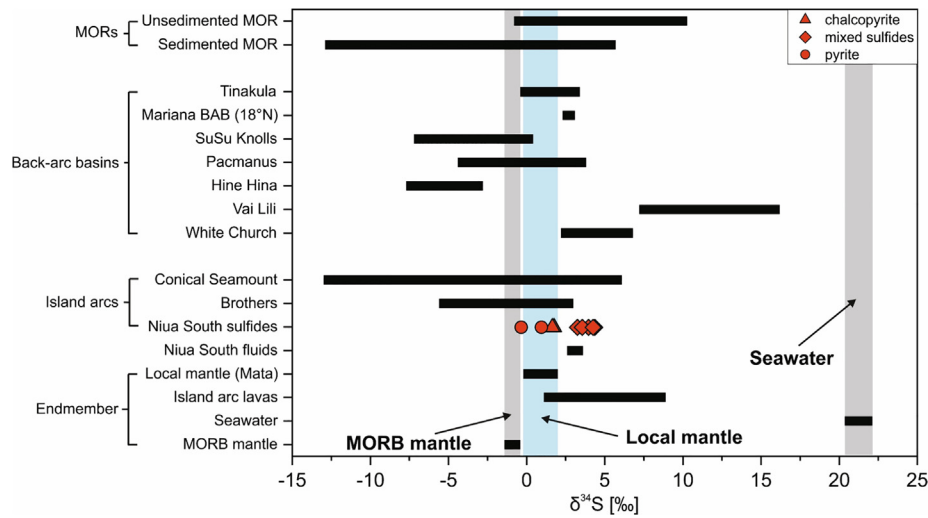
Fig. 9. Comparison of the $\delta^{34}S$ data from the Niua South sulfide separates with mid-ocean ridge (Shanks and Seyfried, 1987; Hannington and Scott, 1988; Woodruff and Shanks, 1988; Knott et al., 1995; Butler et al., 1998; Friedman, 1998; Gemmell et al., 2004; Rouxel et al., 2004), back-arc (Kusakabe et al., 1990; Herzig et al., 1998; Kim et al., 2004; Anderson et al., 2019), and island arc submarine hydrothermal systems (Gemmell et al., 2004; de Ronde et al., 2011). The $\delta^{34}S$ composition of modern day seawater (21.24 ± 0.88‰, Tostevin et al., 2014) and MORB (-0.90 ± 0.50‰, Labidi et al., 2012, 2014) is presented by the grey shaded areas and the local mantle composition (-0.2 to 2.0‰, Keller et al., 2009) is presented by the blue shaded area. Reference data for the hydrothermal fluids are from Gartman et al. (2019) and for the island arc rocks from Ueda and Sakai (1984), Woodhead et al. (1987), Alt et al. (1993) and Hoog et al. (2001). (For interpretation of the references to colour in this figure legend, the reader is referred to the web version of this article.)
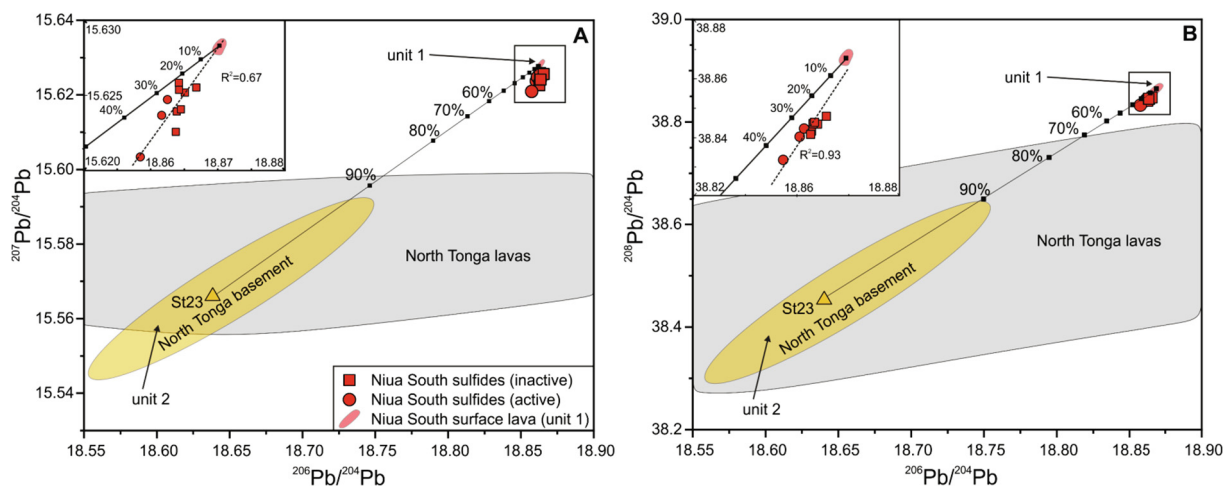

Fig. 10. (A) $^{207}Pb/^{204}Pb$ vs. $^{206}Pb/^{204}Pb$ and (B) $^{208}Pb/^{204}Pb$ vs. $^{206}Pb/^{204}Pb$ for pyrite, chalcopyrite, and mixed sulfide separates from Niua South. Mixing model is based on the mean Pb isotope composition of the dacitic surface lavas (unit 1, electronic supplement Table A5) and a basaltic andesite from the Tonga fore-arc (unit 2; sample St23 from Falloon et al., 2007). The compositional fields of unit 1 and unit 2 represent the range of Pb isotope composition from two and three samples, respectively. Sampling positions of igneous host rocks are highlighted in Fig. 1B. Reference Pb isotope values of the north Tonga lavas includes data from Regelous et al. (1997), Wendt et al. (1997) and Ewart et al. (1998). Insets show the (A) moderate ($R^2 = 0.67$) and (B) strong ($R^2 = 0.93$) positive correlation between the surface lavas and the Niua South hydrothermal sulfides. (For interpretation of the references to colour in this figure legend, the reader is referred to the web version of this article.)

2013; Deditius and Reich, 2016; Román et al., 2019). High concentrations of lattice-bound trace elements in pyrite may particularly occur in arsenian pyrite, where As^- typically substitutes for S^- (Deditius et al., 2014; Keith et al., 2018). Differences in the covalent radii of As (119 pm) and S (105 pm) may cause lattice distortion and S vacancies, which enhances the incorporation of heavier and larger

elements like Au (136 pm) and Te (138 pm) by increasing the accommodation capacity of the crystal lattice for these elements (Reich et al., 2005; Deditius et al., 2014; Keith et al., 2018a, 2020). Trace elements like Ag, Sb, Te, Au, Tl, and Pb typically form a triangular wedge-shaped compositional field in pyrite as a function of As (grey dashed line in Fig. 7A–F) and compositions outside the wedge

Table 5
Paragenetic sequence for the hydrothermal mineralization at Niua South. Mineral abundance estimated by optical microscopy, SEM and XRD (c.f. Table 2 and Fig. 3).

Stage / Mineral	Hydrothermal evolution				Description
	Stage 1 — low T. (<250°C)	Stage 2 — high T. (250-300°C)	Stage 3A — fluid boiling (~318°C)	Stage 3B — liquid upwelling (<280°C)	
Pyrite I	▬▬				Framboids; rapid precipitation, seawater-fluid mixing
Pyrite II		▬▬			Euhedral; in chalcopyrite
Pyrite III			▬▬		Euhedral; inclusion-rich overprinting chalcopyrite
Pyrite mas / Marcasite				- - - (inferred)	Recrystallization of pyrite
Chalcopyrite II		▬▬	dendritic - - -		Overprinting stage 1, massive and disseminated
Native Au / Electrum		▬ - - -	- - -	▬	Micron-sized inclusions in cpy II and sph III
Bi-telluride		▬ - -			Needle-shaped inclusions in cpy II linings
Bornite / Covellite / Chalcocite / Hematite		·····		·········	Supergene secondaries and/or alteration
Sphalerite I	▬▬		dendritic - - -		Dendritic; overgrowing barite, inclusion-rich
Sphalerite III				▬	Coating early stages
Galena	- - -			▬	Colloform and inclusions in sphalerite I and III
Tennantite-Tetrahedrite	- - -			- - ·	
Barite ± anhydrite	▬▬				Euhedral plates; dendritic and rosette textures
Orpiment	- - - - -			- - - - -	Anhedral coating over sulphates and sphalerite

Legend:
— Minor <5 %
— Common 5-25 %
▬ Abundant 25-50%
▬ Dominant >50%
- - - Inferred
········· Supergene alteration

may indicate that inclusions of the respective element are present (Reich et al., 2005; Deditius et al., 2014; Keith et al., 2016, 2018a). However, an inclusion-related incorporation of Ag, Sb, Tl, and Pb may not be generally excluded for analyses within the wedge-shaped zone, since the Au and Te solubility line intersects the wedge (black dashed line in Fig. 7A and B; Reich et al., 2005; Keith et al., 2018a). Gold and Te content in pyrite from Niua South mainly plot below the solubility limit indicating that these elements are primarily hosted in solid solution with only subordinate occurrences of Au and telluride inclusions (Fig. 7A and B). For most other trace elements (e.g., As, Sb, Tl, and Pb), the incorporation at Niua South is less well constrained and concentrations are highly variable over several orders of magnitude between different pyrite generations (Figs. 6 and 7). Time-integrated LA-ICP-MS spectra allows to identify microscale inclusions due to intensity spikes (Wohlgemuth-Ueberwasser et al., 2015; George et al., 2018; Keith et al., 2020). Pyrite I framboids that formed by disequilibrium precipitation and quenching during the early low-temperature stage show such intensity

spikes, which are likely related to inclusions of galena and sphalerite (Fig. 11A and B; Huston et al., 1995; Maslennikov et al., 2009). By contrast, euhedral pyrite II exhibits smooth ablation patterns excluding the occurrence of micro-scale inclusions (Fig. 11C) agreeing with its formation under more stable high-temperature conditions (Huston et al., 1995; Román et al., 2019). By contrast, element concentrations during the boiling stage reached the fluid saturation level due to destabilization of metal complexes, as reflected by inclusions of native Au in pyrite III (Fig. 11D). Late stage, colloform massive pyrites ± marcasite (py mas; Fig. 3G) show low trace element contents (Fig. 6) as a result of dissolution and reprecipitation (Fig. 3G) during low-temperature overprinting and zone refining, indicating that most trace elements are likely hosted in solid solution (Wohlgemuth-Ueberwasser et al., 2015; Grant et al., 2018).

Negative correlations of divalent cations like Fe, Mn, Co, and Cd with Zn in sphalerite indicate an isovalent substitution for Zn^{2+} (Fig. 8A and electric supplement Table A3) (Cook et al., 2009; Keith et al., 2014). However,
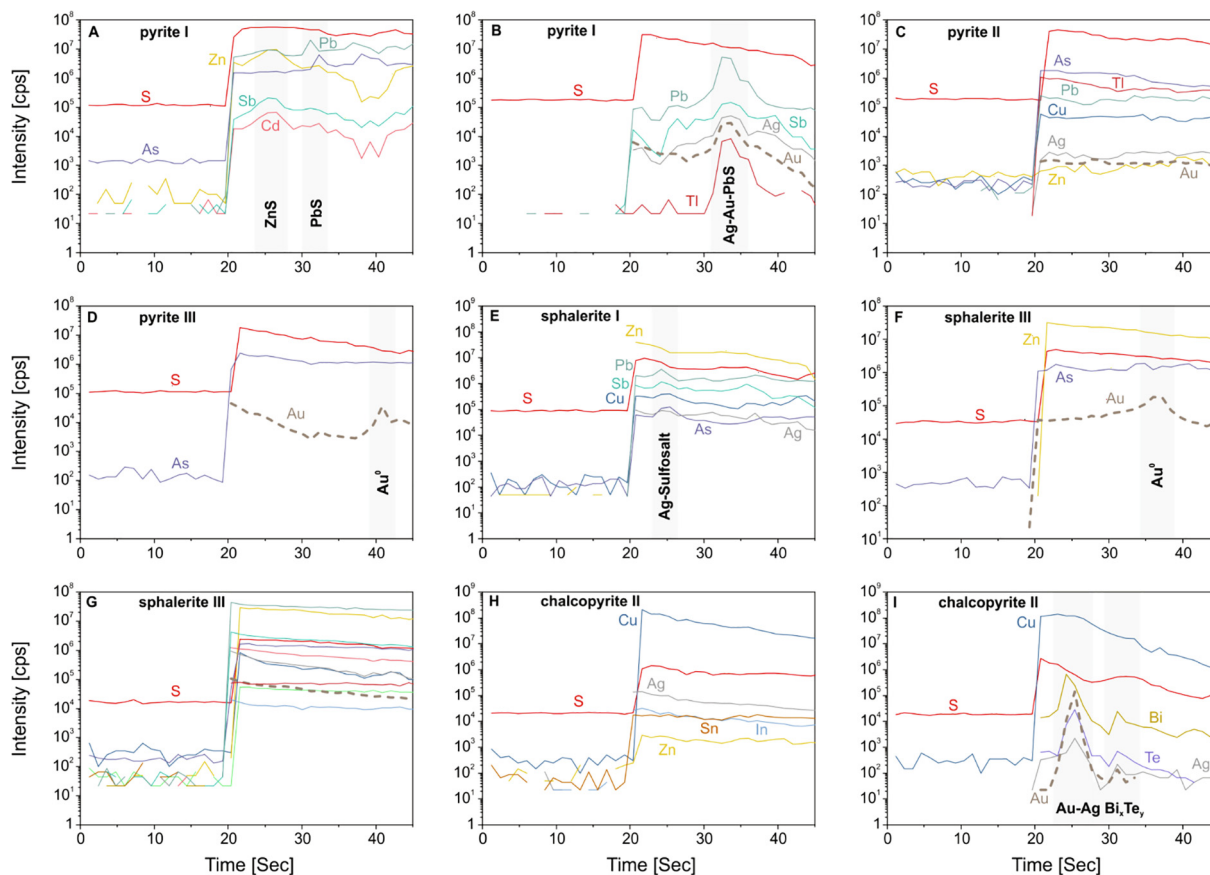
Fig. 11. Representative time-resolved LA-ICP-MS depth profiles of selected trace elements in pyrite (A-D), sphalerite (E-H), and chalcopyrite (H-I). The composition of pyrite I, II, and III analyses in (B) to (D) are highlighted by black circles in Fig. 7. (For interpretation of the references to colour in this figure legend, the reader is referred to the web version of this article.)

elevated Cu contents (>2 wt.%, Table 2) coupled with microscopic evidence for chalcopyrite inclusions in sphalerite I (Barton and Bethke, 1987; Keith et al., 2014) and intensity spikes in the LA-ICP-MS pattern further suggest inclusions of galena and/or Ag-bearing sulfosalts (Fig. 11E). Hence, the hydrothermal fluids were probably supersaturated in Cu, Ag, Sb, and Pb caused by abrupt cooling because of abundant fluid-seawater mixing during the early stage of chimney evolution, as reflected by the early formation of sphalerite I (Table 5). By contrast, late-stage sphalerite III seems to host most trace elements in solid solution as reflected by smooth LA-ICP-MS patterns (Fig. 11G), except the occurrence of native Au and galena inclusions, as revealed by back-scattered electron imaging (Fig. 3O) and intensity spikes (Fig. 11F).

Chalcopyrite II is generally a poor host for most trace elements except Ag, Se, In, and Sn (Fig. 6) and, hence trace elements reaching higher concentration are typically related to inclusions (Huston et al., 1995; Wohlgemuth-Ueberwasser et al., 2015; George et al., 2018), such as the reported native Au and Bi-telluride inclusions (Fig. 3M and N, Fig. 11I). By contrast, the smooth LA-ICP-MS spectra of Ag, Zn, In, Sn, Se, Co, and Ni are consistent with an incorporation in solid solution (Fig. 11H).

We conclude that the trace element incorporation mechanisms in the Niua South sulfides vary with changing fluid conditions, including variable degrees of seawater mixing and fluid boiling preserved by the different paragenetic stages (Table 5).

5.3. Fluid evolution during sulfide precipitation

Similar Au/As and Te/As ratios of pyrite II and III with respect to the Niua South hydrothermal fluids (Fig. 7) indicate that pyrite forming under stable (high-temperature stage 2 and 3A) fluid conditions may reflect the fluid composition (Metz and Trefry, 2000; Maslennikov et al., 2009; Keith et al., 2016). By contrast, pyrite I and massive pyrite show distinct Au/As and Te/As ratios compared to the end-member fluids, which is indicative for a pyrite formation under disequilibrium conditions with respect to the fluid phase likely caused by a strong seawater influx and post-depositional modification, respectively (c.f. Section 5.1). This indicates that the trace element contents of pyrite (I, II, and III) from the different paragenetic stages at Niua South (Table 5) reflect the precipitation conditions from the associated fluid during system evolution, whereas the composition of massive pyrite is affected by metal and

semi-metal remobilization during chimney maturation and may therefore not reflect the original formation conditions (Fig. 12).

Elements like Mn, Ag, Tl, and Pb are typically enriched in the outer, low-temperature parts of sulfide-sulfate chimneys and show higher solubilities in low temperature hydrothermal fluids than elements like Co, Se, In, and Te, which are enriched in the more central parts and exhibit high concentrations in high temperature fluids (Auclair et al., 1987; Butler and Nesbitt, 1999; Metz and Trefry, 2000; Maslennikov et al., 2009). Thus, enrichments of Mn, Ag, Tl, and Pb in pyrite I and/or sphalerite I (stage 1) compared to an enrichment of Co, Se, In, Sn, and Te in chalcopyrite II, pyrite III, and sphalerite III (stage 2 and 3) suggest a fluid temperature increase during chimney maturation from <250 °C to up to 325 °C (Figs. 6 and 12; Auclair et al., 1987; Maslennikov et al., 2009; Revan et al.,

2014; Wohlgemuth-Ueberwasser et al., 2015; Monecke et al., 2016). Selenium/Tl ratios have been used as a temperature proxy in pyrite due to their inverse temperature-dependent behavior in hydrothermal fluids indicating that higher Se/Tl ratios in pyrites reflects higher precipitation temperatures (Auclair et al., 1987; Maslennikov et al., 2009). Cobalt/Ni ratios show an effect similar to Se/Tl ratios, since Co is enriched in high temperature pyrite, whereas Ni either shows no temperature-related variation or reaches high concentrations in pyrite at lower temperatures (e.g., Huston et al., 1995; Maslennikov et al., 2009; Revan et al., 2014; Keith et al., 2016; Meng et al., 2020). Therefore, the positive correlation between Se/Tl and Co/Ni in pyrite ($R^2 = 0.68$; Fig. 7G), as well as the temperature sensitive ratios of Ga/Ge and Fe/Zn in sphalerite ($R^2 = 0.43$; Fig. 8B; Möller, 1987; Keith et al., 2014) further support an evolution from low temperature (<250 °C) to
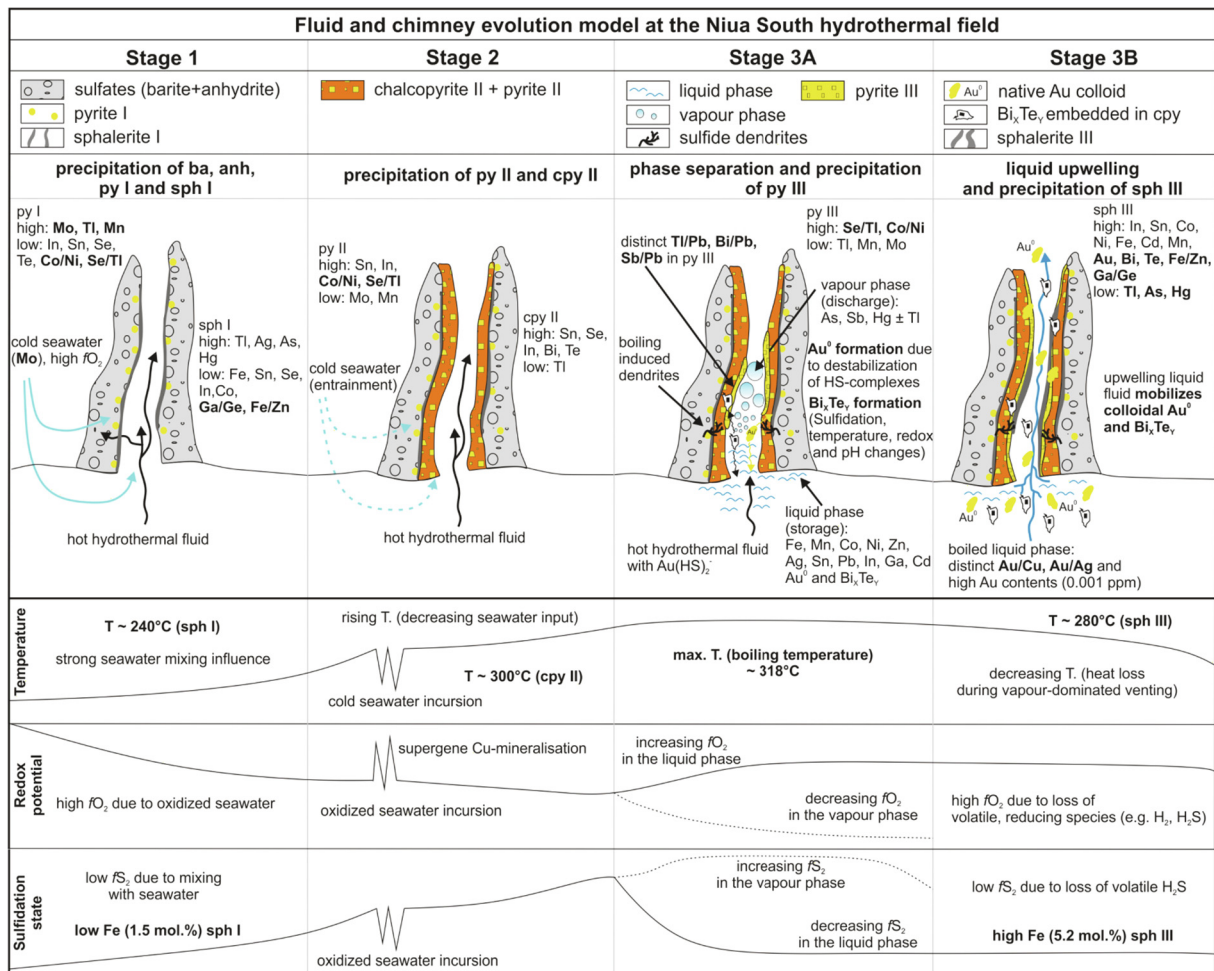

Fig. 12. Fluid and chimney evolution model (not true to scale) for Niua South based on the paragenetic relationships (Table 5) and trace element variations in hydrothermal sulfides (c.f. Section 5.3). Bold font is used for process relevant trace elements and ratios. Stage 1: Extensive mixing of hydrothermal fluid and seawater. Stage 2: Decreasing seawater influx and precipitation under more stable fluid conditions. Stage 3A: Onset of fluid boiling causing metal- and semi-metals fractionation between the vapor and liquid phase accompanied by the formation of native Au, electrum, and Bi-telluride colloids, which are concentrated in a subsurface liquid-dominated fluid layer and incorporated into chalcopyrite II linings and mature pyrite III. Stage 3B: Upwelling of liquid-dominated fluids and adsorption of colloids at the inner chimney wall and incorporation in late-stage sphalerite III. Modified after Meng et al. (2020). (For interpretation of the references to colour in this figure legend, the reader is referred to the web version of this article.)

high-temperature (up to 325 °C) precipitation due to decreasing seawater influence, consistent with the sulfide textures and zoning throughout the chimney walls (c.f. Section 5.1). This is also confirmed by Mo variations in pyrite that can be used as a proxy for seawater mixing, since Mo is depleted in endmember fluids (1–57 nM) compared to seawater (103 nM; Douville et al., 2002; Keith et al., 2016; Meng et al., 2020) Hence, the Mo enrichment in pyrite I framboids, compared to later stage pyrite II and III (Fig. 6) indicate a strong decrease in seawater influence during system maturation (Fig. 12). George et al. (2018) proposed that the Zn/Cd ratio in chalcopyrite can be used to infer its precipitation temperature suggesting that chalcopyrite II (Cd/Zn = 0.007) formed at about 300 °C. This correlates with the temperatures of the discharging fluids (308–318 °C) from the chalcopyrite-pyrite chimneys indicating near boiling conditions at ambient pressure conditions at 1140–1170 m water depth (Table 1; Bischoff and Rosenbauer, 1984; Gartman et al., 2018). Sphalerite formation temperatures inferred by the Fe/Zn ratio (Keith et al., 2014) reveal slightly lower formation temperatures for sphalerite I (240 ± 15 °C) compared to sphalerite III (282 ± 42 °C), which are consistent with the suggested temperature evolution and sphalerite textures with respect to chimney zoning and maturation (Fig. 12; Haymon, 1983; Tivey et al., 1999; Berkenbosch et al., 2012). The temperature drop in stage 3B is suggested to be the result of heat loss during fluid boiling and vapor-dominated venting in stage 3A (Monecke et al., 2014).

Sphalerite compositions, in combination with mineral assemblages and formation temperatures, can be used to reconstruct the sulfidation state of a hydrothermal system (Einaudi et al., 2003; Keith et al., 2014; Kawasumi and Chiba, 2017). Iron contents in sphalerite I (G.M. = 1.5 m ol%) and sphalerite III (5.2 mol.%) as well as the absence of pyrrhotite are indicative for intermediate sulfidation conditions above the pyrite-pyrrhotite equilibrium (Fig. 13), which is supported by the occurrence of tennantite-tetrahedrite and orpiment (Table 2; Einaudi et al., 2003). Increasing fS_2 during stage 1 to higher fS_2 during stage 2 and 3A can be inferred due to increasing fluid temperatures and decreasing fluid-seawater mixing affecting the redox and sulfidation potential of the hydrothermal fluids (Kawasumi and Chiba, 2017). Higher temperatures and fS_2 conditions during stage 3A (Table 5) may be achieved by venting of H_2S-rich vapor-dominated fluids produced by fluid boiling during stage 3A (Figs. 12 and 13; Drummond and Ohmoto, 1985; Cooke and McPhail, 2001). Sulfur fugacity and temperature apparently decreased towards stage 3B (Fig. 13), which can be related to the upwelling of Cl-rich and H_2S-poor liquid-dominated fluids (c.f. Section 5.1 and Fig. 13). These Cl-rich fluids likely formed during fluid boiling, that was associated with heat and H_2S loss to the vapor phase during stage 3A (Figs. 12 and 13; Drummond and Ohmoto, 1985; Monecke et al., 2014). We conclude that the mineralogy of the hydrothermal sulfides and the trace element composition of pyrite, sphalerite, and chalcopyrite from the different paragenetic stages can effectively trace the evolution of different physicochemical fluid parameters (temperature, fO_2 and fS_2) during chimney maturation and fluid boiling
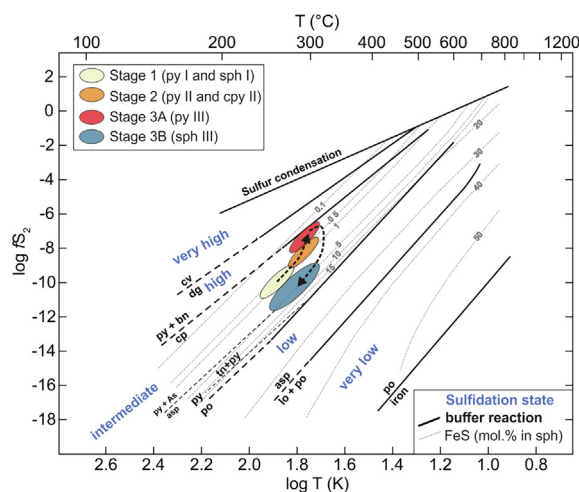

Fig. 13. Log fS_2 – 1000/T diagram with mineral sulfidation reactions at 1 bar. Mineral stabilities and mol.% FeS in sphalerite indicate increasing fS_2 from stage 1 to stage 3A, followed by a drastic drop in fS_2 induced by the extensive loss of H_2S during fluid boiling (c.f. Section 5.1 and Fig. 12). Modified after Einaudi et al. (2003). (For interpretation of the references to colour in this figure legend, the reader is referred to the web version of this article.)

in submarine arc-related hydrothermal systems (Figs. 12 and 13).

5.4. Effects of phase separation and colloidal transport

"Vapor flames" of discharging fluids (Fig. 2G) and fluid salinities (up to 695 mM Cl; Table 1), which exceed seawater values (540 mM Cl, Millero et al., 2008) provide evidence for Cl-rich liquid-dominated venting at Niua South (Coumou et al., 2009; Monecke et al., 2014; Gartman et al., 2018, 2019). Fluid samples with salinities lower than seawater (453 mM Cl) observed by Gartman et al. (2019), occurring on different sample sites in the vent field suggest a co-occurrence of vapor- and liquid-dominated hydrothermal fluids within the Niua South system. The co-existence of low salinity vapors and high salinity liquids within the same hydrothermal field suggests a continuous boiling process leading to a more saline and dense liquid-dominated layer in the subsurface associated with the condensation of low-density vapor into seawater at the seafloor (Coumou et al., 2009).

Ratios of trace elements in pyrite with a vapor (e.g., Sb, Tl, Bi) and liquid (e.g., Pb) affinity can provide important insights into boiling processes (Román et al., 2019) and can help to define the onset of fluid boiling at Niua South. Low Tl/Pb (<0.02), Bi/Pb (<0.03), and Sb/Pb (<0.5) ratios in pyrite III (±II) at Niua South are comparable to pyrite from a boiling horizon in the Cerro Pabellón geothermal system (Fig. 7H and I; Román et al., 2019) and are a result of Tl, Bi, and Sb loss to the vapor phase. Hence, pyrite III likely formed directly from a boiling fluid and may therefore define the onset of the boiling stage (stage 3A) at Niua South (Table 5, Fig. 12), which agrees with the paragenetic sulfide relations and textures (c.f. Section 5.1). By contrast, sphalerite III (stage 3B) shows a distinct enrichment in ele-

ments with a liquid affinity that typically form Cl-complexes (e.g., Co, Ni, Cd, In, Sn), and a depletion in elements with a vapor affinity (e.g., As, Hg, Tl) compared to sphalerite I, which is likely related to a previous element loss to the vapor phase in stage 3A (Table 4, Fig. 6) (Pokrovski et al., 2002; Pokrovski et al., 2013; Román et al., 2019). We propose that sphalerite III formation is related to the precipitation from an upwelling intermediate-temperature (~280 °C) (c.f. Section 5.3), high salinity (595–695 mM Cl, Table 1) liquid-dominated fluid from a liquid layer beneath the boiling horizon (Coumou et al., 2009; Monecke et al., 2014).

The Cl-rich fluids from Niua South show Au contents (up to 1 ppb Au; Gartman et al., 2018, 2019) comparable to other Au-rich fluids from boiling geothermal systems from the Taupo volcanic zone (up to 2.3 ppb Au; Simmons and Brown, 2007) or the Reykjanes geothermal system (up to 20.9 ppb Au; Hannington et al., 2016), which significantly exceed those from typical mid-ocean ridge hydrothermal systems (up to 0.08 ppb; Fuchs et al., 2019). The Au-rich nature of the hydrothermal fluids at Niua South and Reykjanes have been attributed to native Au colloids, representing an important mechanism for the hydrothermal Au flux in boiling hydrothermal systems (Hannington et al., 2016; Gartman et al., 2018, 2019). Based on the boiling fluid data presented by Gartman et al. (2019), we estimate that up to 63% of the dissolved Au is bisulfide-complexed in the most saline fluids (up to 645.9 mM Cl, Gartman et al., 2019) of Niua South, despite the low H_2S contents (731–2274 μM/L, Haase, 2018) of these fluids. Hence, the dissolved Au contents are near saturation, indicating that cooling and/or further H_2S loss will drive Au precipitation (supplementary material 1). Upon reaching the residual liquid saturation level a boiling-induced Cl-rich liquid can be periodically transported upwards (Coumou et al., 2009), colloids are flushed through the vent orifices (Fig. 12; Gartman et al., 2018, 2019) and are incorporated as inclusions into chalcopyrite II linings (Figs. 3M and N, 11I), sphalerite III (Figs. 3O and 11F) and pyrite III (Fig. 11D) as revealed by time-resolved laser ablation patterns and back-scatter electron imaging. Upwelling of a cooled and degassed Cl-rich fluid, which carries boiling-induced colloids of native Au, electrum, and Au-Bi-tellurides led to the high Au contents in the sulfide-sulfate chimneys (up to >30 ppm; Table 3) at Niua South (Gartman et al., 2018). Similar precious (Au) and volatile (e.g., As, Sb) element enrichments observed at the NW caldera vent field of Brothers volcano (Kermadec arc) are related to a magmatic volatile influx increasing the content of these elements in the hydrothermal fluids (de Ronde et al., 2011). The input of magmatic volatiles into a hydrothermal circulation cell typically results in a low fluid pH, as known, for example, from Brothers (1.9–3.4, de Ronde et al., 2011, 2019) as well as DESMOS and SuSu Knoll in the eastern Manus basin (0.9–2.1, Seewald et al., 2015). However, at Niua South evidence for a magmatic volatile influx is lacking (c.f. Section 5.5) and, hence, the partly low pH (3.1–7.9, Table 1) values at Niua South and the precious and volatile element enrichment in the seafloor sulfides are rather the result of vapor–liquid element fractionation caused by fluid boiling. Experimental results by Ballhaus et al. (2019) imply that Cl-rich liquid-dominated fluids that formed by boiling may show pH values as low as 2.8, which are comparable to the lowest pH values (>3.1) observed at Niua South (Table 1). Thus, we propose that such boiling-induced element enrichment processes are particularly important for shallow (<1500 mbsl) submarine arc-related hydrothermal systems, since fractionation and precipitation processes related to fluid boiling are more efficient at lower temperatures and pressure conditions (Drummond and Ohmoto, 1985; Monecke et al., 2014) and can drastically alter the precious (Au) and volatile (As, Sb, Se, Te, Tl) element budget in hydrothermal precipitates, even if a magmatic volatile influx is lacking (c.f. Section 5.5).

5.5. Constraints on sulfur- and metal sources

Stable (δ^{34}S) and radiogenic isotopes (^{206}Pb/^{204}Pb, ^{207}Pb/^{204}Pb, ^{208}Pb/^{204}Pb) allow us to define the sulfur- and metal source(s) of the hydrothermal fluids and their sulfide precipitates (Fouquet and Marcoux, 1995; Herzig et al., 1998; Verati et al., 1999; Kim et al., 2004; Ono et al., 2007; McDermott et al., 2015; Martin et al., 2020). Sulfide in submarine hydrothermal systems may be derived from bacterial/biogenic (<150 °C) or thermochemical (>160 °C) reduction of seawater sulfate (δ^{34}S = 21.24 ± 0.88‰; Tostevin et al., 2014), leaching from igneous rocks with various δ^{34}S compositions, or the disproportion of magmatically derived SO_2 (Herzig et al., 1998; Kim et al., 2004; Ono et al., 2007; Martin et al., 2020). The δ^{34}S range (−0.3 to 4.4‰) of hydrothermal sulfides from Niua South (Fig. 9) exclude a biogenic source for S, since highly negative δ^{34}S values are lacking and the effect of biogenic reduction can be neglected in high temperature hydrothermal systems like Niua South (Table 1; Ono et al., 2007; McDermott et al., 2015). The contribution of magmatic volatiles to a hydrothermal systems typically leads to δ^{34}S values in the fluids and related sulfide precipitates that are lower than in the related host rocks (Herzig et al., 1998; Ono et al., 2007; McDermott et al., 2015; Martin et al., 2020). The δ^{34}S composition of Tonga arc lavas is unknown, however, δ^{34}S analyses of volcanic glass samples (−0.2 to 2‰, Keller et al., 2009) from the nearby Mata volcano in the NE Lau basin provide an estimation of the local δ^{34}S composition at Niua South. This assumption is reasonable, since 1) Mata volcano is located <10 km to the west of Niua South (Fig. 1B), 2) the observed δ^{34}S variations at Mata volcano is distinctly higher than the δ^{34}S composition of mid-ocean ridge basalts (δ^{34}S = −0.90 ± 0.50‰; Labidi et al., 2012, 2014), and 3) the δ^{34}S values from Mata volcano overlap with global island arc rocks (5.0 ± 3.9‰, Ueda and Sakai, 1984; Woodhead et al., 1987; Alt et al., 1993; Hoog et al., 2001) (Fig. 9). Hence, the S isotope composition of the hydrothermal Niua South sulfides (−0.3 to 4.4‰) likely reflects an igneous host rock source for S (−0.2 to 2‰, Keller et al., 2009) combined with minor contribution of thermochemical reduced seawater S (δ^{34}S = 21.24 ± 0.88‰; Tostevin et al., 2014). The proportions of S derived from these reservoirs can be estimated by

the two component mixing model introduced by Ono et al. (2007). Considering that only the inner chalcopyrite lining ($\delta^{34}S$ = 1.7 to 1.8‰) may be in equilibrium with the hydrothermal fluids (McDermott et al., 2015; Evans et al., 2020) we estimate that S leached from the host rocks ($\delta^{34}S$ = −0.2 to 2.0‰, mean 1.1‰) in the reaction and upflow zone mixed with less than 5% of seawater derived S ($\delta^{34}S$ = 21.24 ± 0.88‰; Figs. 12 and 14). Alternatively, similar $\delta^{34}S$ values in hydrothermal sulfides can be produced by "anhydrite buffering" (Ono et al., 2007). However, multiple S isotope data of fluid H_2S from Niua South exclude this process, as well as the contribution of isotopically light S by magmatic volatiles (Gartman et al., 2019), which confirms our conclusion that most of the S in the sulfide precipitates is of host rock and seawater origin. Mixed sulfide separates, sampled from the outer sulfate-rich chimney wall, show elevated $\delta^{34}S$ (3.6–4.4‰) compared to pyrite or chalcopyrite, which is conclusive with in-situ $\delta^{34}S$ zonation patterns from the inner to the outer chimney wall observed by Meng et al. (2020) and, thus, records the partly seawater origin of S. The $\delta^{34}S$ composition of pyrite (−0.3 to 1.0‰) lies in the typical range of 1.0–1.5‰ of sulfide-fluid H_2S isotope fractionation (Shanks III, 2001; Ono et al., 2007) overlapping with values of equilibrium-chalcopyrite and with the local mantle values. Ratios of Se/S*10^6 in pyrite and bulk sulfide samples are also commonly used to define the source of S and Se in hydrothermal systems and ratios >1500 are suggested to be related to a magmatic volatile influx (Huston et al., 1995; Layton-Matthews et al., 2008; Martin et al., 2019, 2021). All the Se/S×10^6 values in the pyrite and bulk sulfide

data from Niua South are consistently below the magmatic threshold (supplementary material 1), providing further evidence that the hydrothermal system was not affected by a magmatic volatile influx.

Host rock leaching during hydrothermal circulation seems to be the dominant metal and semi-metal source at Niua South and, thus, the Pb isotope signature of the hydrothermal sulfides can be used to trace the contributions of different source rocks to the metal budget (Fouquet and Marcoux, 1995; Zeng et al., 2017). Small, but statistically relevant differences between the Pb isotope composition of the Niua South surface dacitic lavas (unit 1: electronic supplement Table A5) and hydrothermal sulfides exist and suggest an additional less radiogenic Pb source in the reaction zone of the hydrothermal system (Figs. 10 and 14). During fluid circulation the Pb isotope signal is homogenized and, thus, the sulfides represent a mixture of the respective Pb isotope reservoirs (Fouquet and Marcoux, 1995; Verati et al., 1999). Basaltic andesites from the Tonga fore-arc (unit 2) in the immediate vicinity of Niua volcano (e.g., sample St23 from Falloon et al., 2007; Fig. 1B) are less radiogenic than the Niua South surface dacites and may therefore represent an analogue to the host rocks in the deeper reaction zone (Figs. 10 and 14). Hence, Pb from two distinct reservoirs including 1) the younger surface dacites (unit 1) and 2) the older basement basaltic andesites (unit 2) likely explain the Pb isotope composition of the Niua South hydrothermal sulfides (Fig. 14). Our mixing calculation, which is based on the mean Pb isotope composition of unit 1 (electronic supplement Table A5) and unit 2 (sample St23 from Falloon et al., 2007) suggest that 20 to 40% of the
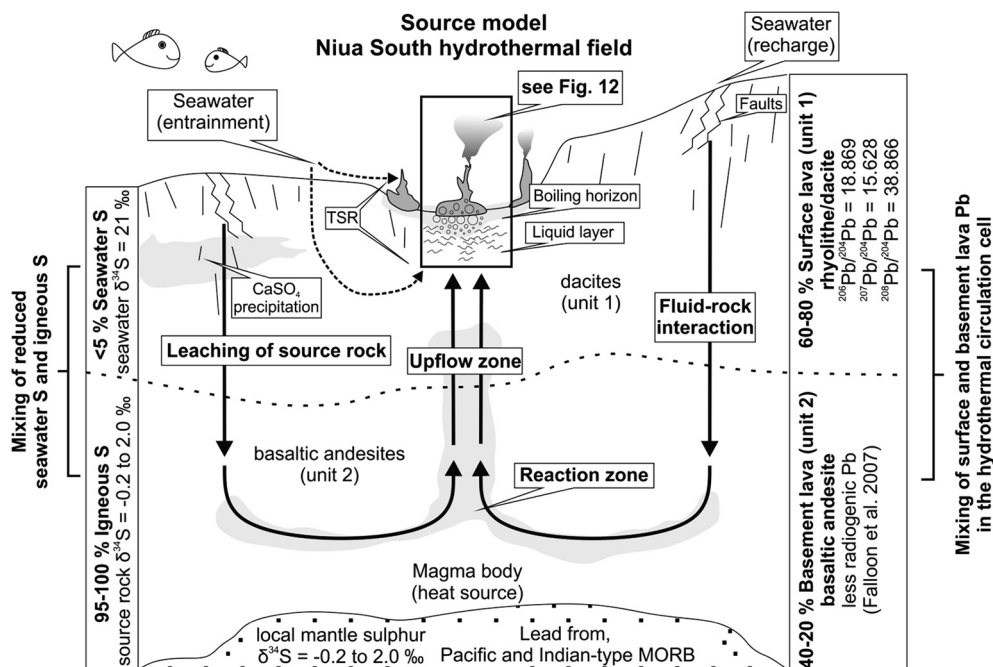

Fig. 14. Model (not true to scale) for the Niua South vent field including key hydrothermal processes and source components. The detailed precipitation and fluid boiling processes are illustrated in Fig. 12. Modified after McDermott et al. (2015). Abbreviations: TSR = thermochemical sulfate reduction. (For interpretation of the references to colour in this figure legend, the reader is referred to the web version of this article.)

total Pb was derived from the basement rocks (unit 2) in the reaction zone, whereas 60 to 80% was leached during fluid ascent from the (near)-surface dacites (unit 1) in the upflow zone (Figs. 10 and 14). Although the thickness of the isotopically distinct rock units is unknown, our results indicate that the more radiogenic upper layer (unit 1) contributes more to the Pb isotope signatures of the hydrothermal sulfides than the deeper less radiogenic section (unit 2). Hence, we conclude that most of the S, Se, and Pb, as well as related metals and semi-metals were leached from the igneous host rock in the reaction zone and hydrothermal upflow zone, and that a contribution by magmatic volatiles is unlikely.

6. SUMMARY AND CONCLUSIONS

We examined the bulk sulfide, stable S isotope, radiogenic Pb isotope, and in-situ mineral composition of hydrothermal precipitates from the boiling Niua South vent site to develop a comprehensive model for volatile and precious element enrichment in boiling arc-related submarine hydrothermal systems. Boiling-induced trace element fractionation in hydrothermal fluids has been long recognized, however, its effect on the sulfide composition is still poorly constrained. At Niua South chemical variations between hydrothermal sulfides from different paragenetic stages are generally more distinct than between active and inactive chimney samples, which implies that large scale hydrothermal processes and/or source components were similar over the lifetime of the circulation system with only short-term changes in physicochemical fluid parameters (e.g., temperature, pH, fS_2, and fO_2) in response to seawater-mixing and fluid boiling.

Sub-samples of different zones from active and inactive vents at Niua South were subdivided into chalcopyrite-pyrite samples representing the more central parts of the chimney structure, sphalerite-barite samples from the outer chimney wall and pyrite-marcasite massive sulfide talus. Sulfides that host numerous inclusions (e.g., Au^0, Bi_xTe_y, electrum) together with dendritic intergrowth are interpreted to have formed by quenching as a result of seawater mixing (stage 1) and boiling-induced precipitation (stage 3) due to supersaturation of fluid in metal- and semi-metal species. Euhedral and pristine sulfides formed under stable high temperature fluid conditions in stage II. The evolution from a low-temperature (<250 °C, stage I) to high-temperature (up to 325 °C, stage 3A) system from the outer chimney wall to the central fluid conduit reflects the maturation of the chimney structures and has consequences for the mineral textures and trace element composition of pyrite (e.g., Se/Tl, Co/Ni, Mo) and sphalerite (e.g., Fe/Zn, Ga/Ge) from the different paragenetic stages. Differences in the FeS content of early sphalerite I (stage I) and late sphalerite III (stage 3B) reveals changes in the sulfidation state of the hydrothermal systems due to H_2S loss during fluid boiling in the mature chimney stage (stage 3A). Inclusion-rich crustiform high-temperature pyrite III, that precipitated during the boiling stage (stage 3A), shows characteristically low Bi/Pb (<0.03), Tl/Pb (<0.02), and Sb/Pb (<0.5) ratios as a results of boiling-induced element

fractionation. By contrast, late-stage sphalerite III is enriched in elements like Mn, Co, Ni, Ga, Cd, In, and Sn that have an affinity to the Cl-rich liquid phase during fluid boiling, which proposes a late stage upwelling of a Cl-rich liquid-dominated fluid (stage 3B). This liquid may also carry boiling-induced native Au, electrum, and Bi-telluride colloids, which are preserved as inclusions in pyrite III and sphalerite III. Periodic upwelling of this Cl- and Au-rich liquids may represent a common process for extreme Au enrichments (>30 ppm Au) in sulfide-sulfate chimneys in boiling submarine arc-related hydrothermal systems and can have important implications on the formation and exploration of Au-rich SMS and VMS deposits.

Sulfur and Pb isotope data revealed that most metals and semi-metals were likely derived from the host rocks by leaching, whereas evidence for a magmatic volatile influx is lacking compared to many other arc-related submarine hydrothermal systems. Consequently, our results demonstrate that volatile (e.g., As, Sb, Se, Te), and precious (Au) element enrichment in submarine arc-related hydrothermal systems can be decoupled from a magmatic volatile influx and is instead a result of boiling-induced trace element fractionation – a hydrothermal enrichment process, which has been underestimated to date.

Declaration of Competing Interest

The authors declare that they have no known competing financial interests or personal relationships that could have appeared to influence the work reported in this paper.

APPENDIX A. SUPPLEMENTARY MATERIAL

Supplementary data to this article can be found online at https://doi.org/10.1016/j.gca.2021.05.047.

REFERENCES

Abraitis P. K., Pattrick R. A. and Vaughan D. J. (2004) Variations in the compositional, textural and electrical properties of natural pyrite: a review. *Int. J. Miner. Process.* **74**, 41–59.

Alt J. C., Shanks W. C. and Jackson M. C. (1993) Cycling of sulfur in subduction zones: The geochemistry of sulfur in the Mariana Island Arc and back-arc trough. *Earth Planet. Sci. Lett.* **119**, 477–494.

Anderson M. O., Hannington M. D., McConachy T. F., Jamieson J. W., Anders M. and Wienkenjohann H., et al. (2019) Mineralization and alteration of a modern seafloor massive sulfide deposit hosted in mafic volcaniclastic rocks. *Econ. Geol.* **114**, 857–896.

Arculus R. J. (2006) Northern Tonga Arc and Fonualei Rifts: initial results from the NoToVE (SS11/2004) Research Voyage. *ASEG Extended Abstracts* **2006**, 1–5.

Auclair G., Fouquet Y. and Bohn M. (1987) Distribution of selenium in high-temperature hydrothermal sulfide deposits at 13 degrees North, East Pacific Rise. *Canadian Mineral.* **25**, 577–587.

Ballhaus C., Gäb F., Garbe-Schönberg D. and Staubwasser M. (2019) Effect of boiling on the acidity of hydrothermal solutions. *Contrib. Miner. Petrol.* **174**, 2.

Barton P. B. and Bethke P. M. (1987) Chalcopyrite disease in sphalerite: pathology and epidemiology. *Am. Mineral.* **72**, 451–467.

Beaulieu S. E., Szafrański K. M. (2020). InterRidge Global Database of Active Submarine Hydrothermal Vent Fields Version 3.4.

Berkenbosch H. A., de Ronde C. E. J., Gemmell J. B., McNeill A. W. and Goemann K. (2012) Mineralogy and Formation of Black Smoker Chimneys from Brothers Submarine Volcano, Kermadec Arc. *Econ. Geol.* **107**, 1613–1633.

Bevis M., Taylor F. W., Schutz B. E., Recy J., Isacks B. L. and Helu S., et al. (1995) Geodetic observations of very rapid convergence and back-arc extension at the Tonga arc. *Nature* **374**, 249–251.

Bischoff J. L. and Rosenbauer R. J. (1984) The critical point and two-phase boundary of seawater, 200–500 C. *Earth Planet. Sci. Lett.* **68**, 172–180.

Butler I. B., Fallick A. E. and Nesbitt R. W. (1998) Mineralogy, sulphur isotope geochemistry and the development of sulphide structures at the Broken Spur hydrothermal vent site, 29° 10'N, Mid-Atlantic Ridge. *J. Geol. Soc.* **155**, 773–785.

Butler I. B. and Nesbitt R. W. (1999) Trace element distributions in the chalcopyrite wall of a black smoker chimney: insights from laser ablation inductively coupled plasma mass spectrometry (LA–ICP–MS). *Earth Planet. Sci. Lett.* **167**, 335–345.

Ciobanu C. L., Cook N. J. and Spry P. G. (2006) Preface-Special Issue: Telluride and selenide minerals in gold deposits-how and why?. *Mineral. Petrol.* **87**, 163.

Compston W. and Oversby V. M. (1969) Lead isotopic analysis using a double spike. *J. Geophys. Res.* **74**, 4338–4348.

Cooke D. R. and McPhail A. (2001) Epithermal Au-Ag- Te mineralization, Acupan, Baguio district, Philippines: numerical simulations of mineral deposition. *Econ. Geol.* **96**, 109–131.

Cook N. J., Ciobanu C. L., Pring A., Skinner W., Shimizu M. and Danyushevsky L., et al. (2009) Trace and minor elements in sphalerite: A LA-ICPMS study. *Geochim. Cosmochim. Acta* **73**, 4761–4791.

Corliss J. B., Dymond J., Gordon L. I., Edmond J. M., Herzen R. P. V. and Ballard R. D., et al. (1979) Submarine Thermal Springs on the Galápagos Rift. *Science* **203**, 1073–1083.

Coumou D., Driesner T., Weis P. and Heinrich C. A. (2009) Phase separation, brine formation, and salinity variation at Black Smoker hydrothermal systems. *J. Geophys. Res.* **114**, 1108.

de Ronde C. E. J., Massoth G. J., Butterfield D. A., Christenson B. W., Ishibashi J. and Ditchburn R. G., et al. (2011) Submarine hydrothermal activity and gold-rich mineralization at Brothers Volcano, Kermadec Arc, New Zealand. *Miner. Deposita* **46**, 541–584.

de Ronde C. E. J., Humphris S. E., Höfig T. W. and Reyes A. G. IODP Expedition 376 Scientists (2019) Critical role of caldera collapse in the formation of seafloor mineralization. The case of Brothers volcano.. *Geology* **47**, 762–766.

Deditius A. P., Reich M., Kesler S. E., Utsunomiya S., Chryssoulis S. L., Walshe J. and Ewing R. C. (2014) The coupled geochemistry of Au and As in pyrite from hydrothermal ore deposits. *Geochim. Cosmochim. Acta* **140**, 644–670.

Deditius A. P. and Reich M. (2016) Constraints on the solid solubility of Hg, Tl, and Cd in arsenian pyrite. *Am. Mineral.* **101**, 1451–1459.

Dekov V. M., Bindi L., Burgaud G., Petersen S., Asael D. and Rédou V., et al. (2013) Inorganic and biogenic As-sulfide precipitation at seafloor hydrothermal fields. *Mar. Geol.* **342**, 28–38.

Doebelin N. and Kleeberg R. (2015) Profex: a graphical user interface for the Rietveld refinement program BGMN. *J. Appl. Crystallogr.* **48**, 1573–1580.

Douville E., Charlou J. L., Oelkers E. H., Bienvenu P., Colon C. J. and Donval J. P., et al. (2002) The rainbow vent fluids (36 14′ N, MAR) the influence of ultramafic rocks and phase separation on trace metal content in Mid-Atlantic Ridge hydrothermal fluids. *Chem. Geol.* **184**, 37–48.

Drummond S. E. and Ohmoto H. (1985) Chemical evolution and mineral deposition in boiling hydrothermal systems. *Econ. Geol.* **80**, 126–147.

Einaudi M. T., Hedenquist J. W. and Inan E. E. (2003) Sulfidation state of fluids in active and extinct hydrothermal systems: Transitions from porphyry to epithermal environments. *Special Publ.-Soc. Econ. Geol.* **10**, 285–314.

Embley R. W. and Rubin K. H. (2018) Extensive young silicic volcanism produces large deep submarine lava flows in the NE Lau Basin. *Bull. Volcanol.* **80**, 36.

Evans G. N., Tivey M. K., Monteleone B., Shimizu N., Seewald J. S. and Rouxel O. J. (2020) Trace element proxies of seafloor hydrothermal fluids based on secondary ion mass spectrometry (SIMS) of black smoker chimney linings. *Geochim. Cosmochim. Acta* **269**, 346–375.

Ewart A., Collerson K. D., Regelous M., Wendt J. I. and Niu Y. (1998) Geochemical evolution within the Tonga–Kermadec–Lau arc–back-arc systems: the role of varying mantle wedge composition in space and time. *J. Petrol.* **39**, 331–368.

Falloon T. J., Danyushevsky L. V., Crawford T. J., Maas R., Woodhead J. D. and Eggins S. M., et al. (2007) Multiple mantle plume components involved in the petrogenesis of subduction-related lavas from the northern termination of the Tonga Arc and northern Lau Basin: evidence from the geochemistry of arc and backarc submarine volcanics. *Geochem. Geophys. Geosyst.* **8**.

Fouquet Y. and Marcoux E. (1995) Lead isotope systematics in Pacific hydrothermal sulfide deposits. *J. Geophys. Res. Solid Earth* **100**, 6025–6040.

Fouquet Y., Henry K., Knott R. and Cambon P. (1998) Geochemical section of the TAG hydrothermal mound. *Oceanogr. Literature Rev.* **8**, 1356.

Franklin J. M., Gibson H. L., Galley A. G. and Jonasson I. R. (2005). Economic Geology, 100th Anniversary Volume.

Friedman C. T. (1998) *Analysis of stable sulfur isotopes and trace cobalt on sulfides from the TAG hydrothermal mound.* Massachusetts Institute of Technology.

Fuchs S., Hannington M. D. and Petersen S. (2019) Divining gold in seafloor polymetallic massive sulfide systems. *Miner. Deposita* **54**, 789–820.

Gartman A. and Luther, III, G. W. (2013) Comparison of pyrite (FeS2) synthesis mechanisms to reproduce natural FeS2 nanoparticles found at hydrothermal vents. *Geochim. Cosmochim. Acta* **120**, 447–458.

Gartman A., Hannington M., Jamieson J. W., Peterkin B., Garbe-Schönberg D. and Findlay A. J., et al. (2018) Boiling-induced formation of colloidal gold in black smoker hydrothermal fluids. *Geology* **46**, 39–42.

Gartman A., Findlay A. J., Hannington M., Garbe-Schönberg D., Jamieson J. W. and Kwasnitschka T. (2019) The role of nanoparticles in mediating element deposition and transport at hydrothermal vents. *Geochim. Cosmochim. Acta* **261**, 113–131.

GEBCO Bathymetric Compilation Group (2020). The GEBCO_2020 Grid - a continuous terrain model of the global oceans and land.

Gemmell J. B., Sharpe R., Jonasson I. R. and Herzig P. M. (2004) Sulfur isotope evidence for magmatic contributions to submarine and subaerial gold mineralization: conical Seamount and the Ladolam gold deposit, Papua New Guinea. *Econ. Geol.* **99**, 1711–1725.

George L. L., Cook N. J., Crowe B. B. P. and Ciobanu C. L. (2018) Trace elements in hydrothermal chalcopyrite. *Mineral. Mag.* **82**, 59–88.

Grant H. L., Hannington M. D., Petersen S., Frische M. and Fuchs S. H. (2018) Constraints on the behavior of trace elements in the actively-forming TAG deposit, Mid-Atlantic Ridge, based on LA-ICP-MS analyses of pyrite. *Chem. Geol.* **498**, 45–71.

Haase K.M. (2018). In cooperation with Shipboard Scientific Party: SO-263 Cruise Report: Tonga Rift.

Hannington M., Harðardóttir V., Garbe-Schönberg D. and Brown K. L. (2016) Gold enrichment in active geothermal systems by accumulating colloidal suspensions. *Nat. Geosci.* **9**, 299.

Hannington M., Jamieson J., Monecke T., Petersen S. and Beaulieu S. (2011) The abundance of seafloor massive sulfide deposits. *Geology* **39**, 1155–1158.

Hannington M. D. and Scott S. D. (1988) Mineralogy and geochemistry of a hydrothermal silica-sulfide-sulfate spire in the caldera of Axial Seamount, Juan de Fuca Ridge. *Canadian Mineral.* **26**, 603–625.

Hannington M. D., de Ronde C. and Petersen S. (2005). Sea-floor tectonics and submarine hydrothermal systems. In Economic Geology 100th Anniversary Volume, vol. 1905, 111–141.

Haymon R. M. (1983) Growth history of hydrothermal black smoker chimneys. *Nature* **301**, 695.

Hekinian R., Fevrier M., Bischoff J. L., Picot P. and Shanks W. C. (1980) *Sulfide Deposits from the East Pacific Rise Near 21 {degrees}N*. Science (New York, N.Y.), pp. 1433–1444.

Herzig P. M., Hannington M. D. and Arribas, Jr, A. (1998) Sulfur isotopic composition of hydrothermal precipitates from the Lau back-arc: implications for magmatic contributions to seafloor hydrothermal systems. *Miner. Deposita* **33**, 226–237.

de Hoog J. C., Taylor B. E. and Van Bergen M. J. (2001) Sulfur isotope systematics of basaltic lavas from Indonesia: implications for the sulfur cycle in subduction zones. *Earth Planet. Sci. Lett.* **189**, 237–252.

Huston D. L., Sie S. H., Suter G. F., Cooke D. R. and Both R. A. (1995) Trace elements in sulfide minerals from eastern Australian volcanic-hosted massive sulfide deposits; Part I, Proton microprobe analyses of pyrite, chalcopyrite, and sphalerite, and Part II, Selenium levels in pyrite; comparison with delta 34 S values and implications for the source of sulfur in volcanogenic hydrothermal systems. *Econ. Geol.* **90**, 1167–1196.

Kawasumi S. and Chiba H. (2017) Redox state of seafloor hydrothermal fluids and its effect on sulfide mineralization. *Chem. Geol.* **451**, 25–37.

Keith M., Haase K. M., Schwarz-Schampera U., Klemd R., Petersen S. and Bach W. (2014) Effects of temperature, sulfur, and oxygen fugacity on the composition of sphalerite from submarine hydrothermal vents. *Geology* **42**, 699–702.

Keith M., Häckel F., Haase K. M., Schwarz-Schampera U. and Klemd R. (2016) Trace element systematics of pyrite from submarine hydrothermal vents. *Ore Geol. Rev.* **72**, 728–745.

Keith M., Smith D. J., Jenkin G. R. T., Holwell D. A. and Dye M. D. (2018a) A review of Te and Se systematics in hydrothermal pyrite from precious metal deposits: Insights into ore-forming processes. *Ore Geol. Rev.* **96**, 269–282.

Keith M., Haase K. M., Klemd R., Smith D. J., Schwarz-Schampera U. and Bach W. (2018b) Constraints on the source of Cu in a submarine magmatic-hydrothermal system, Brothers volcano. *Kermadec island arc. Contr. Mineral. Petrol.* **173**, 40.

Keith M., Smith D. J., Doyle K., Holwell D. A., Jenkin G. R. T. and Barry T. L., et al. (2020) Pyrite chemistry: a new window into Au-Te ore-forming processes in alkaline epithermal districts, Cripple Creek, Colorado. *Geochim. Cosmochim. Acta* **274**, 172–191.

Keith M., Haase K. M., Häckel F., Schwarz-Schampera U., Klemd R. and Hannington M., et al. (2021) Trace element fractionation and precipitation in submarine back-arc hydrothermal systems, Nifonea caldera, New Hebrides subduction zone. *Ore Geol. Rev.*, 104211.

Keller N. S., Rubin K. H., Clague D. A., Michael P. J., Resing J. A., Cooper L. B. et al. (2009). Sulfur in submarine eruptions: Observations and preliminary data from West Mata, NE Lau Basin. In American Geophysical Union, Fall Meeting, V43I-08.

Kilias S. P., Nomikou P., Papanikolaou D., Polymenakou P. N., Godelitsas A. and Argyraki A., et al. (2013) New insights into hydrothermal vent processes in the unique shallow-submarine arc-volcano, Kolumbo (Santorini), Greece. *Scientific reports* **3**, 2421.

Kim J., Lee I. and Lee K.-Y. (2004) S, Sr, and Pb isotopic systematics of hydrothermal chimney precipitates from the Eastern Manus Basin, western Pacific: evaluation of magmatic contribution to hydrothermal system. *J. Geophys. Res.* **109**.

Klevenz V., Bach W., Schmidt K., Hentscher M., Koschinsky A. and Petersen S. (2011) Geochemistry of vent fluid particles formed during initial hydrothermal fluid–seawater mixing along the Mid-Atlantic Ridge. *Geochem. Geophys. Geosyst.* **12**.

Knott R., Fallick A. E., Rickard D. and Bäcker H. (1995) Mineralogy and sulphur isotope characteristics of a massive sulphide boulder, Galapagos Rift, 85 55′ W. *Geol. Soc., London, Special Publ.* **87**, 207–222.

Kristall B., Kelley D. S., Hannington M. D. and Delaney J. R. (2006) Growth history of a diffusely venting sulfide structure from the Juan de Fuca Ridge: a petrological and geochemical study. *Geochem. Geophys. Geosyst.* **7**.

Kusakabe M., Mayeda S. and Nakamura E. (1990) S, O and Sr isotope systematics of active vent materials from the Mariana backarc basin spreading axis at 18 N. *Earth Planet. Sci. Lett.* **100**, 275–282.

Kwasnitschka T. (2016): Cruise FK160320 on RV Falkor. Virtual Vents. With assistance of Schmidt Ocean Institute.

Labidi J., Cartigny P., Birck J. L., Assayag N. and Bourrand J. J. (2012) Determination of multiple sulfur isotopes in glasses: A reappraisal of the MORB δ34S. *Chem. Geol.* **334**, 189–198.

Labidi J., Cartigny P., Hamelin C., Moreira M. and Dosso L. (2014) Sulfur isotope budget (32S, 33S, 34S and 36S) in Pacific-Antarctic ridge basalts: A record of mantle source heterogeneity and hydrothermal sulfide assimilation. *Geochim. Cosmochim. Acta* **133**, 47–67.

Layton-Matthews D., Peter J. M., Scott S. d. and Leybourne M. I. M. I. (2008) Distribution, mineralogy, and geochemistry of selenium in felsic volcanic-hosted massive sulfide deposits of the Finlayson Lake district, Yukon Territory, Canada. *Econ. Geol.* **103**, 61–88.

Libbey R. B. and Williams-Jones A. E. (2016) Relating sulfide mineral zonation and trace element chemistry to subsurface processes in the Reykjanes geothermal system, Iceland. *J. Volcanol. Geoth. Res.* **310**, 225–241.

Lupton J. (2008). In cooperation with Shipboard Scientific Party: TN227 on RV Thomas G. Thompson. Accessed 31.08.2020 http://www.pmel.noaa.gov/eoi/laubasin/documents/tn227-nelau-report-final.pdf.

Lupton J., Rubin K. H., Arculus R., Lilley M., Butterfield D. and Resing J., et al. (2015) Helium isotope, C/3He, and Ba-Nb-Ti signatures in the northern Lau Basin: distinguishing arc, back-arc, and hotspot affinities. *Geochem. Geophys. Geosyst.* **16**, 1133–1155.

Martin A. J., Keith M., McDonald I., Haase K. M., McFall K. A., Klemd R. and MacLeod C. J. (2019) Trace element systematics and ore-forming processes in mafic VMS deposits: evidence from the Troodos ophiolite, Cyprus. *Ore Geol. Rev.* **106**, 205–225.

Martin A. J., Keith M., Parvaz D. B., McDonald I., Boyce A. J. and McFall K. A., et al. (2020) Effects of magmatic volatile influx in mafic VMS hydrothermal systems: evidence from the Troodos ophiolite, Cyprus. *Chem. Geol.* **531**, 119–325.

Martin A. J., McDonald I., Jenkin G. R. T., McFall K. A., Boyce A. J., Jamieson J. W. and MacLeod C. J. (2021) A missing link between ancient and active mafic-hosted seafloor hydrothermal systems–Magmatic volatile influx in the exceptionally preserved Mala VMS deposit, Troodos. *Cyprus. Chem. Geol.* 120127.

Maslennikov V. V., Maslennikova S. P., Large R. R. and Danyushevsky L. V. (2009) Study of trace element zonation in vent chimneys from the Silurian Yaman-Kasy volcanic-hosted massive sulfide deposit (Southern Urals, Russia) using laser ablation-inductively coupled plasma mass spectrometry (LA-ICPMS). *Econ. Geol.* **104**, 1111–1141.

McDermott J. M., Ono S., Tivey M. K., Seewald J. S., Shanks W. C. and Solow A. R. (2015) Identification of sulfur sources and isotopic equilibria in submarine hot-springs using multiple sulfur isotopes. *Geochim. Cosmochim. Acta* **160**, 169–187.

Melekestseva I. Y., Tret'yakov G. A., Nimis P., Yuminov A. M., Maslennikov V. V. and Maslennikova S. P., et al. (2014) Barite-rich massive sulfides from the Semenov-1 hydrothermal field (Mid-Atlantic Ridge, 13 30.87′ N): Evidence for phase separation and magmatic input. *Mar. Geol.* **349**, 37–54.

Meng X., Li X., Chu F., Zhu J., Lei J. and Li Z., et al. (2020) Trace element and sulfur isotope compositions for pyrite across the mineralization zones of a sulfide chimney from the East Pacific Rise (1–2°S). *Ore Geol. Rev.* **116** 103209.

Merle S., Resing J., Embley R., Crowhurst P., Tontini F. C. and Chadwick B., et al. (2012) in cooperation with shipboard scientific crew: Submarine Ring of Fire 2006 (SRoF-12) Northeast Lau Basin, R/V Roger Revelle Expedition RR1211, Captain Wes Hill, Sept 9–25 2012, Suva Fijy to Apia Samoa. *NOAA*, 1–260.

Metz S. and Trefry J. H. (2000) Chemical and mineralogical influences on concentrations of trace metals in hydrothermal fluids. *Geochim. Cosmochim. Acta* **64**, 2267–2279.

Millero F. J., Feistel R., Wright D. G. and McDougall T. J. (2008) The composition of standard seawater and the definition of the reference-composition salinity scale. *Deep Sea Res. Part I* **55**, 50–72.

Möller P. (1987) Correlation of homogenization temperatures of accessory minerals from sphalerite-bearing deposits and Ga/Ge model temperatures. *Chem. Geol.* **61**, 153–159.

Monecke T., Petersen S., Hannington M. D., Grant H. and Samson I. (2016) The minor element endowment of modern sea-floor massive sulfide deposits and comparison with deposits hosted in ancient volcanic successions. *Rev. Econ. Geol.* **18**, 245–306.

Monecke T., Petersen S. and Hannington M. D. (2014) Constraints on water depth of massive sulfide formation: evidence from modern seafloor hydrothermal systems in arc-related settings. *Econ. Geol.* **109**, 2079–2101.

Münch U., Blum N. and Halbach P. (1999) Mineralogical and geochemical features of sulfide chimneys from the MESO zone, Central Indian Ridge. *Chem. Geol.* **155**, 29–44.

Murowchick J. B. and Barnes H. L. (1987) Effects of temperature and degree of supersaturation on pyrite morphology. *Am. Mineral.* **72**, 1241–1250.

Ono S., Shanks W. C., Rouxel O. J. and Rumble D. (2007) S-33 constraints on the seawater sulfate contribution in modern seafloor hydrothermal vent sulfides. *Geochim. Cosmochim. Acta* **71**, 1170–1182.

Pašava J., Vymazalová A. and Petersen S. (2007) PGE fractionation in seafloor hydrothermal systems: examples from mafic- and ultramafic-hosted hydrothermal fields at the slow-spreading Mid-Atlantic Ridge. *Miner. Deposita* **42**, 423–431.

Pokrovski G. S., Zakirov I. V., Roux J., Testemale D., Hazemann J.-L., Bychkov A. Y. and Golikova G. V. (2002) Experimental study of arsenic speciation in vapor phase to 500°C: implications for As transport and fractionation in low-density crustal fluids and volcanic gases. *Geochim. Cosmochim. Acta* **66**, 3453–3480.

Pokrovski G. S., Borisova A. Y. and Bychkov A. Y. (2013) Speciation and transport of metals and metalloids in geological vapors. *Rev. Mineral. Geochem.* **76**, 165–218.

Pokrovski G. S., Akinfiev N. N., Borisova A. Y., Zotov A. V. and Kouzmanov K. (2014) Gold speciation and transport in geological fluids: Insights from experiments and physical-chemical modelling. *Geol. Soc. London, Special Publ.* **402**, 9–70.

Reed M. H. (2006) Sulfide mineral precipitation from hydrothermal fluids. *Rev. Mineral. Geochem.* **61**, 609–631.

Reeves E. P., Seewald J. S., Saccocia P., Bach W., Craddock P. R. and Shanks W. C., et al. (2011) Geochemistry of hydrothermal fluids from the PACMANUS, Northeast Pual and Vienna Woods hydrothermal fields, Manus basin, Papua New Guinea. *Geochim. Cosmochim. Acta* **75**, 1088–1123.

Regelous M., Collerson K. D., Ewart A. and Wendt J. I. (1997) Trace element transport rates in subduction zones: evidence from Th, Sr and Pb isotope data for Tonga-Kermadec arc lavas. *Earth Planet. Sci. Lett.* **150**, 291–302.

Reich M., Kesler S. E., Utsunomiya S., Palenik C. S., Chryssoulis S. L. and Ewing R. C. (2005) Solubility of gold in arsenian pyrite. *Geochim. Cosmochim. Acta* **69**, 2781–2796.

Reich M., Deditius A., Chryssoulis S., Li J.-W., Ma C.-Q. and Parada M. A., et al. (2013) Pyrite as a record of hydrothermal fluid evolution in a porphyry copper system: a SIMS/EMPA trace element study. *Geochim. Cosmochim. Acta* **104**, 42–62.

Reich M., Román N., Barra F. and Morata D. (2020) Silver-Rich Chalcopyrite from the Active Cerro Pabellón Geothermal System, Northern Chile. *Minerals* **10**, 113.

Revan M. K., Genç Y., Maslennikov V. V., Maslennikova S. P., Large R. R. and Danyushevsky L. V. (2014) Mineralogy and trace-element geochemistry of sulfide minerals in hydrothermal chimneys from the Upper-Cretaceous VMS deposits of the eastern Pontide orogenic belt (NE Turkey). *Ore Geol. Rev.* **63**, 129–149.

Román N., Reich M., Leisen M., Morata D., Barra F. and Deditius A. P. (2019) Geochemical and micro-textural fingerprints of boiling in pyrite. *Geochim. Cosmochim. Acta* **246**, 60–85.

Rona P. A., Hannington M. D., Raman C. V., Thompson G., Tivey M. K. and Humphris S. E., et al. (1993) Active and relict sea-floor hydrothermal mineralization at the TAG hydrothermal field, Mid-Atlantic Ridge. *Econ. Geol.* **88**, 1989–2017.

Rouxel O., Fouquet Y. and Ludden J. N. (2004) Subsurface processes at the Lucky Strike hydrothermal field, Mid-Atlantic Ridge: evidence from sulfur, selenium, and iron isotopes. *Geochim. Cosmochim. Acta* **68**, 2295–2311.

Rubin K. H., Embley R. W., Arculus R. J. and Lupton J. E. (2013). Magmatically Greedy Reararc Volcanoes of the N. Tofua Segment of the Tonga Arc. In AGU Fall Meeting Abstracts.

Seewald J. S., Reeves E. P., Bach W., Saccocia P. J., Craddock P. R. and Shanks W. C., et al. (2015) Submarine venting of magmatic volatiles in the Eastern Manus Basin, Papua New Guinea. *Geochim. Cosmochim. Acta* **163**, 178–199.

Shanks, III, W. C. (2001) Stable isotopes in seafloor hydrothermal systems: vent fluids, hydrothermal deposits, hydrothermal alteration, and microbial processes. *Rev. Mineral. Geochem.* **43**, 469–525.

Shanks W. C. and Seyfried W. E. (1987) Stable isotope studies of vent fluids and chimney minerals, southern Juan de Fuca Ridge: Sodium metasomatism and seawater sulfate reduction. *J. Geophys. Res. Solid Earth* **92**, 11387–11399.

Simmons S. F. and Brown K. L. (2007) The flux of gold and related metals through a volcanic arc, Taupo Volcanic Zone, New Zealand. *Geology* **35**, 1099–1102.

Smith I. E. and Price R. C. (2006) The Tonga-Kermadec arc and Havre-Lau back-arc system: their role in the development of tectonic and magmatic models for the western Pacific. *J. Volcanol. Geoth. Res.* **156**, 315–331.

Storch B., Haase K. M., Romer R. H. W., Beier C. and Koppers A. A. P. (2020) Rifting of the oceanic Azores Plateau with episodic volcanic activity. *Sci. Rep.* **10**, 19718.

Sylvester Paul Josep (2001) *Laser-ablation-ICPMS in the earth sciences: principles and applications*. Mineralogical Association of Canada.

Tardani D., Reich M., Deditius A. P., Chryssoulis S., Sánchez-Alfaro P., Wrage J. and Roberts M. P. (2017) Copper–arsenic decoupling in an active geothermal system: A link between pyrite and fluid composition. *Geochim. Cosmochim. Acta* **204**, 179–204.

Tivey M. K., Stakes D. S., Cook T. L., Hannington M. D. and Petersen S. (1999) A model for growth of steep-sided vent structures on the Endeavour Segment of the Juan de Fuca Ridge: results of a petrologic and geochemical study. *J. Geophys. Res.* **104**, 22859–22883.

Tivey M. K. (2007) Generation of seafloor hydrothermal vent fluids and associated mineral deposits. *Oceanography* **20**, 50–65.

Tostevin R., Turchyn A. V., Farquhar J., Johnston D. T., Eldridge D. L., Bishop J. K. and McIlvin M. (2014) Multiple sulfur isotope constraints on the modern sulfur cycle. *Earth Planet. Sci. Lett.* **396**, 14–21.

Ueda A. and Sakai H. (1984) Sulfur isotope study of Quaternary volcanic rocks from the Japanese Islands Arc. *Geochim. Cosmochim. Acta* **48**, 1837–1848.

Ueno H., Hamasaki H., Murakawa Y., Kitazono S. and Takeda T. (2003) Ore and gangue minerals of sulfide chimneys from the North Knoll, Iheya Ridge, Okinawa Trough, Japan. *JAMSTEC J. Deep Sea Res.* **22**, 49–62.

van Achterbergh E., Ryan C. G. and Griffin W. L. (2001) *GLITTER on-line interactive data reduction for the LA-ICPMS microprobe*. Macquarie Research Ltd., Sydney.

Verati C., Lancelot J. and Hékinian R. (1999) Pb isotope study of black-smokers and basalts from Pito Seamount site (Easter microplate). *Chem. Geol.* **155**, 45–63.

Wang S., Li H., Zhai S., Yu Z., Shao Z. and Cai Z. (2017) Mineralogical characteristics of polymetallic sulfides from the Deyin-1 hydrothermal field near 15 S, southern Mid-Atlantic Ridge. *Acta Oceanolog. Sin.* **36**, 22.

Webber A. P., Roberts S., Murton B. J. and Hodgkinson M. R. S. (2015) Geology, sulfide geochemistry and supercritical venting at the Beebe Hydrothermal Vent Field, Cayman Trough. *Geochem. Geophys. Geosyst.* **16**, 2661–2678.

Wendt J. I., Regelous M., Collerson K. D. and Ewart A. (1997) Evidence for a contribution from two mantle plumes to island-arc lavas from northern Tonga. *Geology* **25**, 611.

Wohlgemuth-Ueberwasser C. C., Viljoen F., Petersen S. and Vorster C. (2015) Distribution and solubility limits of trace elements in hydrothermal black smoker sulfides: An in-situ LA-ICP-MS study. *Geochim. Cosmochim. Acta* **159**, 16–41.

Woodhead J. D., Harmon R. S. and Fraser D. G. (1987) O, S, Sr, and Pb isotope variations in volcanic rocks from the Northern Mariana Islands: implications for crustal recycling in intra-oceanic arcs. *Earth Planet. Sci. Lett.* **83**, 39–52.

Woodruff L. G. and Shanks W. C. (1988) Sulfur isotope study of chimney minerals and vent fluids from 21 N, East Pacific Rise: hydrothermal sulfur sources and disequilibrium sulfate reduction. *J. Geophys. Res. Solid Earth* **93**, 4562–4572.

Xu Q and Scott S. D. (2005). Spherulitic pyrite in seafloor hydrothermal deposits: products of rapid crystallization from mixing fluids. In Mineral deposit research. Meeting the global challenge ; proceedings of the Eighth Biennial SGA Meeting, Beijing, China, 18-21 August 2005: Volume 1 (eds. Frank P. Bierlein and Jingwen Mao), vol. 14. Springer, Berlin (Proceedings of the Eighth Biennial Sga Meeting, Beijing, China, 18 - 21 August 2005), pp. 711–713.

Yang K. and Scott S. d. (2006) Magmatic fluids as a source of metals in seafloor hydrothermal systems. *Washington DC American Geophysical Union Geophysical Monograph Series* **166**, 163–184.

Zeng Z., Ma Y., Chen S., Selby D., Wang X. and Yin X. (2017) Sulfur and lead isotopic compositions of massive sulfides from deep-sea hydrothermal systems: implications for ore genesis and fluid circulation. *Ore Geol. Rev.* **87**, 155–171.

Associate editor: Jun-ichiro Ishibashi